Atmos. Meas. Tech., 19, 2555–2574, 2026
https://doi.org/10.5194/amt-19-2555-2026
© Author(s) 2026. This work is distributed under
the Creative Commons Attribution 4.0 License.

Atmospheric Measurement Techniques
Open Access

Retrieval of global aerosol and surface properties from the Gaofen-5 Directional Polarimetric Camera measurements

Zhenyu Zhang[1], **Jing Li**[1], **Yueming Dong**[1], **Chongzhao Zhang**[1], **Qiurui Li**[1], **and Ling Gao**[2]

[1]Department of Atmospheric and Oceanic Sciences, School of Physics, Peking University, 100871, Beijing, China
[2]National Satellite Meteorological Center, China Meteorological Administration, 100081, Beijing, China

Correspondence: Jing Li (jing-li@pku.edu.cn)

Received: 20 October 2025 – Discussion started: 5 December 2025
Revised: 24 March 2026 – Accepted: 31 March 2026 – Published: 16 April 2026

Abstract. Multi-angle polarimetry has been recognized as the most effective configuration to retrieve aerosol parameters from space. In this study, we developed a numerical inversion algorithm that simultaneously retrieves aerosol optical depth (AOD), single scattering albedo (SSA), and land surface albedo (expressed as the Directional Hemispherical Reflectance, DHR) from multi-angle polarimetric observations of China's Directional Polarimetric Camera (DPC) onboard the Gaofen-5 satellite. As one of the few multi-angle polarimetric sensors in operation, DPC provides multi-spectral polarized measurements at up to 12 viewing angles, offering unique advantages for retrieving multiple aerosol parameters. With sensitivity experiments using the VLIDORT radiative transfer model, we first clarified that SSA retrieval with an uncertainty of 0.03 requires degree of linear polarization (DOLP) observation uncertainties below 0.01 with carefully designed viewing geometries. Subsequently, an optimization-based algorithm was implemented to minimize discrepancies between simulated and observed multi-angle scalar reflectance and DOLP. The algorithm performs well on the simulated dataset, with correlation coefficients of SSA (when AOD > 0.4) reaching 0.65. When laboratory calibration uncertainties representative of the DPC are introduced, retrieval performance degrades accordingly. Retrieval using DPC measurements and validation against AERONET observation also demonstrated robust performance. Retrieved AOD achieved a correlation coefficient of 0.75 with AERONET, comparable to operational satellite products such as those from MODIS. The correlation coefficient of SSA under high aerosol loading (AOD > 0.4) is approximately 0.3, matching the precision of Polarization and Directionality of the Earth's Reflectances instrument (POLDER) SSA products, the previous best satellite-based SSA products. Regional and global results captured spatiotemporal aerosol variability of typical pollution events, including biomass burning plumes and dust transport tracks. The DHR results also align closely with MODIS-derived DHR (bias $= 0.001$). This work not only advances DPC's capability for comprehensive aerosol characterization globally, but also provides a physically interpretable framework for global aerosol and surface monitoring.

1 Introduction

Aerosol properties are of significant importance in both climate change research and atmospheric environmental studies (Albrecht, 1989; Ramanathan et al., 2001; Li et al., 2022a). Satellite remote sensing has emerged as a critical tool for acquiring comprehensive global aerosol observations (Dubovik et al., 2019; Liu et al., 2021). Over the past decades, numerous spaceborne sensors have been employed for global aerosol observation, providing long-term data that serve as crucial references for estimating aerosol radiative effects (Diner et al., 1998; Mishchenko et al., 2007; Torres et al., 2007; Dubovik et al., 2011; Levy et al., 2013). Earlier sensors, such as MODIS, primarily offered single-angle scalar observations for each pixel with limited information content, typically only capable of retrieving column loading of aerosols (Aerosol Optical Depth, AOD) while requiring assumed surface reflectance and other aerosol properties such as Single Scattering Albedo (SSA) which reflects the scattering and absorbing properties of aerosols (Levy et al., 2007b, 2013).

Published by Copernicus Publications on behalf of the European Geosciences Union.

Recently, multi-angle polarimetric sensors could provide both intensity and polarization measurements of radiation at multiple viewing angles for individual pixels, significantly enhancing the information available for the retrieval of aerosol parameters (Dubovik et al., 2019). The multi-angle observations facilitate the separation of surface and aerosol contributions, while polarization signals exhibit heightened sensitivity to aerosol scattering and absorbing properties (Dong et al., 2024). Consequently, multi-angle polarimetric observations have emerged as one of the most promising satellite remote sensing techniques for retrieving a series of aerosol and surface parameters on a global scale (Mishchenko and Travis, 1994; Mishchenko et al., 2010). This potential has been demonstrated by algorithms developed for the world's first operational spaceborne multi-angle polarimetric sensor, Polarization and Directionality of the Earth's Reflectances instrument (POLDER), which achieved comprehensive retrieval of multiple parameters including AOD, SSA, and surface reflectance (Chen et al., 2020; Dubovik et al., 2011; Hasekamp et al., 2011, 2024; Li et al., 2019). These achievements underscore the significant capability of multi-angle polarimetric sensors in advancing aerosol remote sensing. After the retirement of POLDER in 2013, operational spaceborne multi-angle polarimetric observations became limited. The launch of the Directional Polarimetric Camera (DPC) onboard Gaofen-5 in 2018 introduced a new source of multi-angle polarimetric measurements. These observations have supported developments in SSA retrievals in recent years.

The DPC has eight spectral channels spanning 443–910 nm and can provide up to 12 viewing angles, with three channels (490, 670, and 865 nm) offering measurements of both Q and U linear polarization components, theoretically enabling SSA retrieval (Li et al., 2018). Many aerosol retrieval studies based on DPC/GaoFen-5 observations have reported high-quality AOD retrievals (with correlation coefficients up to 0.9 against ground-based measurements; Wang et al., 2021; Jin et al., 2022; Ge et al., 2022). Several studies have also extended the retrieval to additional aerosol optical properties, including SSA. For example, Fang et al. (2022) applied the RemoTAP algorithm to DPC observations to retrieve AOD over China, fine-mode AOD, and SSA over eastern China. Dong et al. (2024) employed machine learning methods to retrieve global land SSA. Jin et al. (2024) implemented the GRASP algorithm for SSA retrieval over ocean from DPC-2/GaoFen-5(02) observations. Ji et al. (2025) and Zhang et al. (2025b) also applied the RemoTAP algorithm to retrieve SSA from DPC-2/GaoFen-5(02) observations. Nevertheless, compared with AOD, global SSA retrievals based on DPC/GaoFen-5 observations have been less frequently reported. Moreover, although machine learning approaches have demonstrated strong performance, they are typically data-driven and rely on the availability of representative training samples, without explicitly modeling the underlying physical mechanisms. As a result, their performance may decrease in regions or conditions with limited observations. On the other hand, studies applying physically based inversion methods to DPC/GaoFen-5 observations for global SSA retrieval are still relatively limited. Further efforts are therefore needed to extend such physically based approaches on the global scale.

This study develops a numerical inversion algorithm based on DPC multi-angle polarimetric observations to retrieve global AOD, SSA, and surface parameters, providing insights into global aerosol and surface properties. The remainder of this paper is organized as follows. Section 2 describes the data, methods, and experiments conducted in this study. Section 3 presents the main results, including sensitivity experiments, validation using simulated data and DPC observations, and regional and global maps of the retrieved parameters. Section 4 discusses the results and concludes the paper.

2 Data and Methods

2.1 DPC Measurements

DPC is China's first operational spaceborne multi-angle polarimetric sensor, successively launched on the Gaofen-5 satellite in May 2018, on Gaofen-5(02) satellite in 2021, and on Daqi-1 satellite in 2022, respectively (Dai et al., 2024; Li et al., 2022b). Although these instruments are based on the same overall design concept, minor differences exist in their specific configurations. This study uses measurements from the DPC instrument onboard the Gaofen-5 satellite launched in May 2018, as the data from the subsequent DPC instruments onboard Gaofen-5(02) and Daqi-1 are not yet well calibrated. The DPC/Gaofen-5 features a spatial resolution of 3.3 km and achieves multi-angle observations of the same target through along-track scanning, with up to 12 viewing angles (typically exceeding 9 angles) for most pixels. The sensor provides measurements across 8 spectral bands (443, 490, 565, 670, 763, 765, 865, and 910 nm) from visible to near-infrared wavelengths, including polarized observations at 490, 670, and 865 nm (Li et al., 2018). Six months of DPC Level 1 data, encompassing April, July, and October 2019, as well as January–March 2020, are used in the retrieval in this study. The AERONET, MODIS, as well as other auxiliary data are selected from the same periods.

The laboratory calibration errors of DPC are within 5 % for normalized radiance and within 0.02 for the degree of linear polarization (DOLP) measurements (Li et al., 2018). However, after launch, DPC exhibited a gradual change in radiometric sensitivity, primarily due to aging of the optical components. This drift is dependent on both wavelength and field of view and can introduce increasing systematic biases if not properly corrected. Studies show potential radiometric drift up to 23 % (Zhu et al., 2022) and DOLP errors possibly exceeding 0.04 (Qie et al., 2021). The radiometric response of DPC is progressively drifting over time and is realted to VZA. Zhu et al. (2022) developed a method based on Rayleigh scattering over the ocean to correct this drift. In deep ocean regions with very low aerosol loading and low surface reflectance, the TOA radiance observed by satellite sensors is dominated by atmospheric Rayleigh scattering, which can be accurately simulated using radiative transfer models. By comparing simulated radiances with DPC observations over such regions, Zhu et al. (2022) provided monthly VZA-dependent calibration coefficients at 443, 490, 565, and 670 nm. The uncertainty associated with the calibration method is about 1 %–7 % (depending on the wavelength and VZA). In this study, these Rayleigh scattering-based calibration coefficients are applied to correct DPC's scalar reflectance at 443, 490, 565, and 670 nm.

2.2 Auxiliary Data

Some auxiliary data are needed to characterize surface reflectance and other related processes. Prior to the inversion process, we matched these auxiliary data with DPC observations. These auxiliary data used in the retrieval are listed in Table 1. Specifically, for land surface, monthly 0.05° NDVI data from MODIS/Aqua observations are matched to calculate surface polarized reflectance. For water surfaces, hourly 0.25° ERA5 global wind speed and wind direction data (Hersbach et al., 2020), monthly ocean salinity data from the GLBu0.08 dataset (Cummings and Smedstad, 2013), and monthly averaged 4 km resolution chlorophyll concentration products from MODIS/Aqua observations are matched to compute the surface reflectance (O'Reilly and Werdell, 2019). Considering the relatively minor influence of aerosol phase matrices on the inversion (Su et al., 2021; Zhang et al., 2024), the phase matrices from the aerosol models clustered by Levy et al. (2007a) are utilized in the retrieval. This approach ensures comprehensive representation of surface and atmospheric conditions, enhancing the accuracy and reliability of the retrieval process.

2.3 AERONET AOD and SSA

The AERONET is a ground-based aerosol remote sensing network, providing long-term observations of aerosol optical and microphysical properties, covering most of the continental areas around the world (Holben et al., 1998). The AERONET AOD observations are derived from direct solar radiation and the SSA products are retrieved from diffuse sky radiance (Dubovik and King, 2000). The AOD measurements are available at multiple wavelengths ranging from 340 to 1640 nm, depending on the site and instrument configuration, whereas the SSA products are provided at four wavelengths at 440, 675, 870 and 1020 nm. These products are very accurate with an AOD uncertainty of 0.01 (visible)–0.02 (UV) and an SSA uncertainty of 0.03 (Giles et al., 2019; Sinyuk et al., 2020), and are often used to validate satellite products. However, as the quality control of Level 2.0 inversion products requires AOD > 0.4, many stations do not have extensive Level 2.0 SSA records. Considering the data quality and data availability, this study utilizes the Version 3 all-point (individual measurement) Level 2.0 AERONET AOD data derived from direct-sun observations, along with quality-controlled Level 1.5 almucantar SSA retrievals from sky radiance measurements. The quality-controlled Level 1.5 SSA are firstly derived from Level 1.5 observations by applying all the Level 2.0 quality control criteria except the AOD threshold (e.g., SZA > 50°, sky error < 5 %, and coincident Level 2.0 AOD measurements). In subsequent sections, different AOD thresholds were applied for screening purposes.

2.4 MODIS Albedo

Since AERONET does not retrieve surface albedo, the validation of the DPC retrieved surface parameters is performed using the daily surafce products from the MCD43C1 dataset which are derived from MODIS/Terra and MODIS/Aqua observations (Schaaf et al., 2002). The MCD43C1 dataset utilizes the RossThick-LiSparse (RTLS) kernel-driven model to characterize land surface reflectance (Schaaf et al., 2002), which can be represented as:

$$\begin{aligned} R_\lambda(\theta_0,\theta,\phi) &= K_{\mathrm{iso}}(\lambda) + K_{\mathrm{vol}} f_{\mathrm{vol}}(\theta_0,\theta,\phi) \\ &\quad + K_{\mathrm{geo}} f_{\mathrm{geo}}(\theta_0,\theta,\phi). \end{aligned} \quad (1)$$

In Eq. (1), the terms $K_{\mathrm{iso}}(\lambda)$, $K_{\mathrm{vol}}(\lambda) f_{\mathrm{vol}}$ and $K_{\mathrm{geo}}(\lambda) f_{\mathrm{geo}}$ represent isotropic, volumetric, and geometric-optical surface scattering at wavelength λ, respectively. Here, $K_{\mathrm{iso}}(\lambda)$, $K_{\mathrm{vol}}(\lambda)$, and $K_{\mathrm{geo}}(\lambda)$ are the spectral intensity parameters of the three components, while $f_{\mathrm{vol}}(\theta_0,\theta,\phi)$ and $f_{\mathrm{geo}}(\theta_0,\theta,\phi)$ are Ross-thick and Li-sparse kernel functions, respectively. In our retrieval algorithm, we utilize the wavelength-dependent RTLS model (Litvinov et al., 2011), which can expressed as:

$$\begin{aligned} & R_\lambda(\theta_0,\theta,\phi) \\ & = K(\lambda)\left[1 + k_{\mathrm{vol}} f_{\mathrm{vol}}(\theta_0,\theta,\phi) + k_{\mathrm{geo}} f_{\mathrm{geo}}(\theta_0,\theta,\phi)\right], \end{aligned} \quad (2)$$

where $K(\lambda)$ is a wavelength dependent intensity parameter, whereas k_{vol} and k_{geo} are wavelength independent parameters. The terms $k_{\mathrm{vol}} K(\lambda)$ and $k_{\mathrm{geo}} K(\lambda)$ in Eq. (2) correspond to $K_{\mathrm{vol}}(\lambda)$ and $K_{\mathrm{geo}}(\lambda)$ in Eq. (1), respectively.

In this study, the Directional Hemispherical Reflectance (DHR, also known as black sky albedo), which represents surface albedo in the absence of atmospheric scattering effects, is computed using the three intensity parameters of the RTLS model (Sinyuk et al., 2007). Considering the differences in the spectral bands between MODIS and DPC observations, the DHR from MODIS is linearly interpolated to the wavelengths of DPC channels. The accuracy of DPC's surface parameter retrievals is evaluated by comparing the retrieved DHR with interpolated MODIS DHR.

Table 1. Auxiliary data used in the research.

Variable	Data Source	Spatial Resolution	Temporal Resolution
NDVI	MODIS/Aqua	0.05°	Monthly
Wind speed and wind direction	ERA5	0.25°	Hourly
Salinity	GLBu0.08	0.08°	Monthly
Chlorophyll concentration	MODIS/Aqua	4 km	Monthly

2.5 VLIDORT Radiative Transfer Model

The Vector LInearized Discrete Ordinate Radiative Transfer (VLIDORT) model is a vector radiative transfer model that accounts for multiple scattering in real atmospheres. It simulates Stokes vectors and their linearized matrices (Jacobians) at arbitrary altitudes and viewing geometries, providing radiative simulations for satellite remote sensing applications and serving as an effective forward model in numerical inversion algorithms (Spurr, 2006). The model allows user-defined atmospheric layering with customizable layer heights and optical properties (including total optical depth, SSA, and Legendre expansion coefficients of phase matrix for both aerosols and gases). It calculates output radiation at selected layers and viewing angles along with corresponding Jacobian matrices with respect to surface parameters and the three key atmospheric optical parameters: AOD, SSA, and phase matrix expansion coefficients. In this study, VLIDORT was employed for sensitivity experiments and served as the forward model in the numerical inversion algorithm.

2.6 Retrieval algorithm

Polarimetric multi-angle observations provide both polarization and angular information, enabling the retrieval of multiple parameters such as AOD, SSA, and surface reflectance from a single pixel. However, the system is strongly nonlinear and high-dimensional, thus the inverse problem is very difficult to solve analytically and should be addressed using iterative numerical approaches.

The relationship between satellite observations and the parameters to be retrieved can be expressed as:

$$\boldsymbol{y} = \mathbf{F}(\boldsymbol{x}) + \boldsymbol{\varepsilon}, \tag{3}$$

where $\boldsymbol{y}$ represents the satellite observations, such as the Stokes vectors at various bands and viewing angles; $\boldsymbol{x}$ is the state vector, which includes the parameters to be retrieved, such as AOD, SSA, and surface reflectance; $\mathbf{F}$ is the forward model, also known as the observation operator, which maps the state vector to the observation space, and is often represented by a radiative transfer model in aerosol retrieval algorithms; and $\boldsymbol{\varepsilon}$ is the error term, encompassing both observation uncertainties and forward model uncertainties. Numerical inversion aims to find a state vector $\hat{\boldsymbol{x}}$ such that $\mathbf{F}(\hat{\boldsymbol{x}})$ closely matches $\boldsymbol{y}$, with $\hat{\boldsymbol{x}}$ being the final retrieval result.

The cost function is constructed as:

$$\begin{aligned} J(\boldsymbol{x}) &= \frac{1}{2}\left[\boldsymbol{y} - \mathbf{F}(\boldsymbol{x})\right]^{\mathrm{T}} \mathbf{S}_{\epsilon}^{-1} \left[\boldsymbol{y} - \mathbf{F}(\boldsymbol{x})\right] \\ &\quad + \frac{1}{2}(\boldsymbol{x} - \boldsymbol{x}_0)^{\mathrm{T}} \mathbf{S}_{\mathrm{a}}^{-1} (\boldsymbol{x} - \boldsymbol{x}_0), \end{aligned} \tag{4}$$

where $\mathbf{S}_{\epsilon}$ is the covariance matrix of observation errors, $\boldsymbol{x}_0$ is the vector of a priori estimates, and $\mathbf{S}_{\mathrm{a}}$ is the covariance matrix of the errors in a priori estimates. The process of solving for $\hat{\boldsymbol{x}}$ based on optimization theory involves minimizing $J(\boldsymbol{x})$. This minimization is achieved through iterative methods, with the direction of each iteration determined by the gradient descent of $J(\boldsymbol{x})$:

$$\nabla_{\boldsymbol{x}} J(\boldsymbol{x}) = -\mathbf{K}^{\mathrm{T}} \mathbf{S}_{\epsilon}^{-1} \left[\boldsymbol{y} - \mathbf{F}(\boldsymbol{x})\right] + \mathbf{S}_{\mathrm{a}}^{-1} (\boldsymbol{x} - \boldsymbol{x}_0). \tag{5}$$

Here, $\mathbf{K}$ is the Jacobian matrix of $\mathbf{F}(\boldsymbol{x})$, representing the partial derivatives of $\mathbf{F}(\boldsymbol{x})$ with respect to the components of $\boldsymbol{x}$:

$$\mathbf{K}_{i,j} = \frac{\partial f_i(\boldsymbol{x})}{\partial x_j}. \tag{6}$$

This iterative approach ensures that the retrieval process converges to a solution that optimally balances the observational data and a priori knowledge, providing robust estimates of the target parameters.

The measurement vector, $\boldsymbol{y}$, is constructed with calibrated scalar reflectance at 443, 490, 565, and 670, as well as DOLP at 490 and 670 nm from several angles. The DOLP is calculated according to Eq. (7):

$$\mathrm{DOLP} = \frac{\sqrt{U^2 + V^2}}{I}. \tag{7}$$

The number of available viewing angles of scalar and polarimetric measurements varies among pixels. However, most pixels are observed from more than 9 viewing angles. Pixels with fewer than 9 viewing angles, which are primarily located near the scan edges, were therefore excluded. For the remaining pixels, observations from the first 9 viewing angles were used in the retrieval to maintain a fixed number of viewing angles for all pixels. Consequently, the scalar reflectance and DOLP at each wavelength consist of measurements acquired from 9 viewing angles. The measurement error covariance matrix, $\mathbf{S}_{\epsilon}^{-1}$, is determined by measurement errors of DPC. Although previous studies have suggested that observational errors of DPC increased after launch (Qie et al., 2021; Zhu et al., 2022), the magnitude of this increase has not been quantitatively characterized. Therefore, this study adopts the official pre-launch laboratory calibration errors, namely 5 % radiance errors and 0.02 DOLP errors (Li et al., 2018), as the observational errors used to construct the measurement error covariance matrix. The usage of DPC measurements and their corresponding error specifications are summarized in Table 2.

The state vector, $\boldsymbol{x}$, is composed of aerosol and surface parameters. Particularly, for land surfaces, the state vector $\boldsymbol{x}$ consists of AOD ($\tau(\lambda)$), SSA ($\omega(\lambda)$), kernel intensity parameters of RTLS model ($K(\lambda)$, k_{vol}, and k_{geo} in Eq. 2), and the scale factor of BPDF-NDVI model (C in Eq. 8), which is used for polarized surface reflectance estimation (Litvinov et al., 2011; Maignan et al., 2009):

$$R_{\mathrm{p}}(\theta_0, \theta, \phi) = \frac{C \exp(-\tan\alpha_I)\exp(-\nu) F_p(\alpha_I, m)}{4(\cos\theta_0 + \cos\theta)}, \qquad (8)$$

where R_{p} is the polarized reflectance, α_I is the incidence angle, ν is the NDVI, m is the refractive index and is fixed to 1.5, and C is the scale factor and is the only free linear parameter of the model. For water surfaces, only $\tau(\lambda)$ and $\omega(\lambda)$ are retrieved as components of the state vector $\boldsymbol{x}$, and the New Cox–Munk model is implemented to compute the surface reflectance (Spurr, 2006). The wavelength-dependent parameters, $\tau(\lambda)$, $\omega(\lambda)$, and $K(\lambda)$, are retrieved at 443, 490, 565, and 670 nm, corresponding to the wavelengths at which DPC observations are used to construct the measurement vector. For AOD and SSA, the a priori state vector and its associated error covariance matrix are prescribed as fixed values, derived from the mean and variance of AERONET measurements. The a priori estimates of surface properties are also fixed, with their errors defined by the corresponding ranges of variability. The use of fixed a priori values is intended to provide a controlled and consistent configuration for evaluating the inherent performance of the retrieval algorithm. Details of the a priori values and associated errors are summarized in Table 3.

An overview of the retrieval algorithm is illustrated in Fig. 1, which mainly involves the following three steps:

1. Data preprocessing. This involves three primary operations: calibration of DPC scalar observations, removing cloud/ice/snow pixels (Dong et al., 2024), and matching auxiliary data (including NDVI, wind speed, salinity, and chlorophyll concentration) with DPC observations. Pixels with glint angle $\leq 40°$ over ocean are also excluded, because enhanced specular reflection at small glint angles reduces the aerosol information content and may introduce geometry-dependent artifacts.

2. Iterative inversion. The calibrated and screened DPC observations, matched auxiliary data, and a priori estimates of target parameters are then fed into the VLIDORT radiative transfer model for iterative inversion.

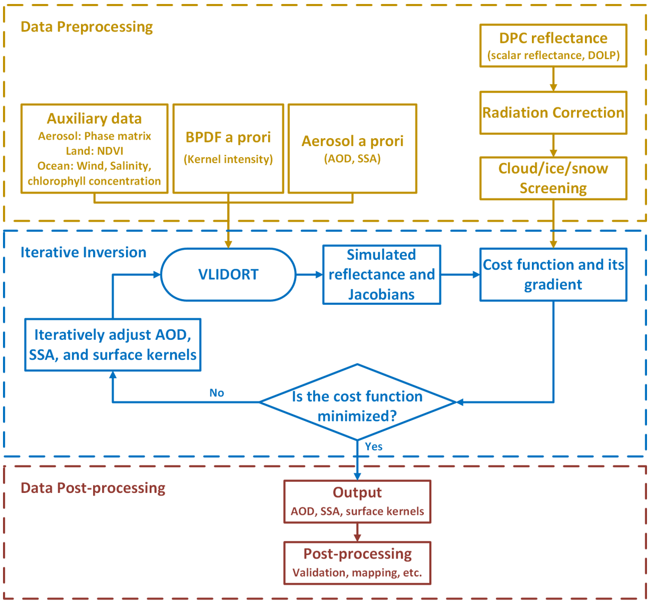

Figure 1. Flowchart for the DPC retrieval algorithm.

The algorithm minimizes the cost function defined in Eq. (4) using an iterative Gauss–Newton method to obtain the final retrieval results.

3. Data post-processing. The retrieved parameters would be screened for further validation and mapping.

2.7 Sensitivity Experiment

To assess an important advantage of multi-angle polarimetry, the capability of SSA retrieval, we first investigate the sensitivity of both scalar and polarized reflectance to SSA. A series of radiative transfer simulations using the VLIDORT model for several DPC channels (443, 490, 565, 670, and 865 nm) under varying geometric parameters was conducted. By perturbing SSA within the AERONET precision (±0.03) under a given set of aerosol and surface models, we analyzed changes in top-of-atmosphere (TOA) scalar and polarized reflectance to evaluate the sensitivity of outgoing radiation to SSA. The 0.03 SSA variation in our sensitivity analysis was chosen for two reasons. First, it corresponds to the reported uncertainty of precise AERONET SSA products, which often serve as a benchmark for validating satellite retrievals (Dubovik et al., 2000; Sinyuk et al., 2020). Second, the requirement to constrain aerosol radiative forcing in climate studies necessitates an SSA uncertainty below 0.03 (GCOS, 2016; Popp et al., 2016). Consequently, this accuracy represents a target for satellite remote sensing of SSA, which has not been met by most available products.

The sensitivity experiments employed the moderately absorbing aerosol model characterized by Levy et al. (2007a) for two distinct surface types, namely vegetation and bare soil, as described by Litvinov et al. (2011). The simulations

Table 2. DPC measurements used for the retrieval.

Measurement	Wavelength	Uncertainty	Number of Angles
Scalar reflectance (I)	443, 490, 565, and 670 nm	5 %	9
DOLP	490 and 670 nm	0.02	9

Table 3. State vector elements, prior values, uncertainty settings, and parameter ranges used in the algorithm.

Parameter	Prior Value	Uncertainty	Range	Description
$\tau(\lambda)$	0.2	0.5	0.001–5.0	Aerosol Optical Depth (AOD)
$\omega(\lambda)$	0.92	0.1	0.7–1.0	Single Scatterin Albedo (SSA)
$K(\lambda)$	0.1	0.3	0.001–0.7	Isotropic parameter in the RTLS model
k_{vol}	0.1	2.0	0.01–5.0	Volumetric parameter in the RTLS model
k_{geo}	0.1	0.4	0.01–0.7	Geometric parameter in the RTLS model
C	6.2	5.0	0.01–10.0	Scale factor of the BPDF-NDVI model

$\lambda = 443$, 490, 565, and 670 nm.

were conducted under a series of SZA, VZA, and RAA, as listed in Table 4. These simulations aim to reveal the observation accuracy required for accurate SSA retrieval from multi-angle polarimetric measurements, and provide guidance for the design of viewing angle.

2.8 Retrieval Experiment Using Simulated Data

Before applying the retrieval algorithm to DPC observations, we conducted a series of retrieval experiments using simulated data to validate the performance of the algorithm. Since the uncertainties of DPC measurement largely exceed laboratory calibration results and are difficult to quantify (Qie et al., 2021; Zhu et al., 2022), the advantage of simulated datasets lies in their controllable radiative errors and the elimination of model uncertainties. The simulated dataset was constructed using aerosol parameters derived from daily AERONET observations selected within an 8 km radius of DPC overpass locations to represent typical aerosol conditions observed by DPC. The corresponding viewing geometry, including SZA, VZA, and RAA, was taken from the matched DPC observations and used in the radiative simulations, thereby accounting for the actual scattering angle distribution of DPC observations. Given that the majority of AERONET stations are located over land, the validation in this study primarily focuses on the retrieval performance for land aerosol and surface parameters. To construct the simulated dataset, DPC observations were first matched with AERONET measurements and MODIS surface parameters (RTLS parameters and NDVI) around the station. Subsequently, a sampling of these matched results was performed, and the sampled AOD, SSA, and surface parameters were used as "true values" to generate TOA scalar and polarized reflectances via VLIDORT simulations. These simulated reflectances were then treated as satellite observations and fed into the retrieval algorithm to retrieve aerosol and surface parameters. Finally, the retrieved parameters were compared with the "true values" used in the simulation to evaluate the inherent retrieval capability of the algorithm. This approach ensures a controlled assessment of the algorithm's performance while minimizing uncertainties arising from the lack of knowledge about actual observational errors.

2.9 Validation of the Retrieval Results

After conducting the sensitivity experiment and the retrieval experiment using simulated data, we applied the retrieval algorithm to DPC observations to derive global AOD, SSA, and DHR. The retrieved products were then systematically evaluated at three spatial scales to assess the algorithm's effectiveness with DPC observations and characterize spatiotemporal variations of aerosol and surface properties. At site scale, the retrieved parameters were spatiotemporally matched with AERONET ground-based measurements for validation. We averaged the retrieved parameters within an 8 km radius of each AERONET station. The AERONET AOD data was selected and averaged within a 30 min window around the DPC overpass, whereas the AERONET daily SSA data was applied to compare against the retrievals. Several widely used statistical indicators, including the correlation coefficient (R), the linear regression equation (slope and intercept), the bias, the mean absolute deviation (MAD), and the root-mean-square error (RMSE), were considered for validation. The regional-scale analysis focused on the algorithm's capability to detect and characterize specific pollution events, including biomass burning episodes and dust outbreaks. Globally, we examined the spatiotemporal patterns of AOD, SSA, and DHR to assess their consistency with known atmospheric processes and surface characteristics.

Table 4. Simulation parameter settings.

Parameter	Values used in Simulations
Wavelength (nm)	443, 490, 565, 670, 865
Solar Zenith Angle (°)	0, 15, 30, 45, 60
Viewing Zenith Angle (°)	0, 15, 30, 45, 60
Relative Azimuth Angle (°)	0, 30, 60, 90, 120, 150, 180
AOD	0.001, 0.1, 0.25, 0.5, 0.75, 1.0, 1.5, 2, 3, 5
SSA	0.8, 0.82, 0.84, 0.86, 0.88, 0.90, 0.92, 0.94, 0.96, 0.98, 1.00
Surface Albedo	0.01, 0.05, 0.1, 0.2, 0.3, 0.5
Scale Factor of BPDF	0.1, 2, 4, 8
NDVI	0.1
Phase Matrix	Moderate, Strong, Weak absorbing type

3 Results

3.1 Sensitivity of Scalar and Polarimetric Measurements to SSA

Figures 2 and 3 present the sensitivity analysis of key aerosol and surface parameters, where Fig. 2 focuses on the scalar reflectance and Fig. 3 further examines the DOLP. Previous studies have already investigated the sensitivity of TOA reflectance to aerosol and surface properties (Su et al., 2021; Sayer et al., 2016), here we also considering sensitivity of DOLP. The results indicate that AOD and surface reflectance exhibit strong sensitivity in both intensity and polarization, suggesting that these quantities are well constrained by the observations. In contrast, the phase matrix shows the weakest sensitivity and is markedly smaller than that of the other parameters, which supports the practical use of a fixed phase matrix in the inversion. SSA shows non-negligible sensitivity, but its magnitude is substantially lower than that of AOD and surface albedo, implying that SSA retrieval is inherently more difficult and more sensitive to observational uncertainties. The sensitivity of the observations to SSA becomes more pronounced at higher AOD, indicating that it is possible to retrieve SSA under high-loading conditions. Given the high sensitivity of the observation geometry, it is therefore necessary to assess the sensitivity of SSA to variations in geometry.

Figures 4 and 5 illustrate the relative changes in TOA scalar reflectance (ΔI) and the changes in DOLP (ΔDOLP) respectively when the SSA varies by ±0.03 under an aerosol loading of $\mathrm{AOD}_{550} = 0.5$. The angular dependence of ΔI and ΔDOLP exhibits comparable behavior for the two different surface types across most bands. Despite minor differences in magnitude and angular distribution, the changes in I and DOLP induced by the prescribed SSA perturbations exhibit similar overall patterns for the two land surface models considered. For all five bands, ΔI has the same sign as ΔSSA, suggesting that an increase (or decrease) in SSA would lead to an increase (or decrease) in scalar reflectance. This aligns with the relationship between SSA and aerosol scattering, thereby affecting scalar reflectance. Overall, as the scattering angle increases, ΔI gradually decreases, indicating reduced sensitivity to SSA.

ΔDOLP also varies with scattering angle, but its response to SSA differs by wavelength (Fig. 5). At scattering angles near 180°, ΔDOLP becomes negligible, indicating low sensitivity to SSA. For the three shorter wavelengths (443, 490, and 565 nm), ΔDOLP exhibits an opposite sign to ΔSSA, decreasing (increasing) with an increase (decrease) in SSA. As the scattering angle decreases from 180°, ΔDOLP first increases and then decreases, reaching its maximum around 90°. Within the scattering angle range of 60–140°, ΔDOLP remains above 0.005 and is relatively sensitive to SSA variations in this range. As the scattering angle further decreases, the magnitude of ΔDOLP also diminishes. The 865 nm band shows negligible ΔDOLP, suggesting minimal sensitivity to SSA at longer wavelength. The behavior of ΔDOLP for the 670 nm band is generally similar to that of the 443, 490, and 565 nm bands, except that ΔDOLP undergoes a sign reversal near 100°. It should be noted that the relationship between ΔDOLP and scattering angle shown in Fig. 5 is based on conditions of $\mathrm{AOD}_{550} = 0.5$ and $\Delta\mathrm{SSA} = \pm 0.03$. Under different aerosol conditions, ΔDOLP may exhibit variations, but the overall trend remains similar. Specifically, shorter wavelengths show more pronounced changes in DOLP, and ΔDOLP follows a more consistent pattern with respect to scattering angle.

It is important to consider the magnitudes of ΔI and ΔDOLP when SSA varies by ±0.03, as they reflect the required observational precision to achieve accurate SSA retrievals with uncertainties of 0.03. Under both vegetation and bare soil conditions with $\mathrm{AOD}_{550} = 0.5$, the magnitudes of ΔI across all bands and scattering angles are generally within 5 %. This range aligns with the typical scalar observation uncertainties of spaceborne sensors, including those of DPC, suggesting that retrieving SSA with 0.03 uncertainty is challenging under a scalar observation uncertainty of 5 %. The values of ΔDOLP are even smaller, with the most sensitive bands showing a change of only 0.01 at 90°. This implies that an SSA retrieval with an uncertainty of 0.03 requires a

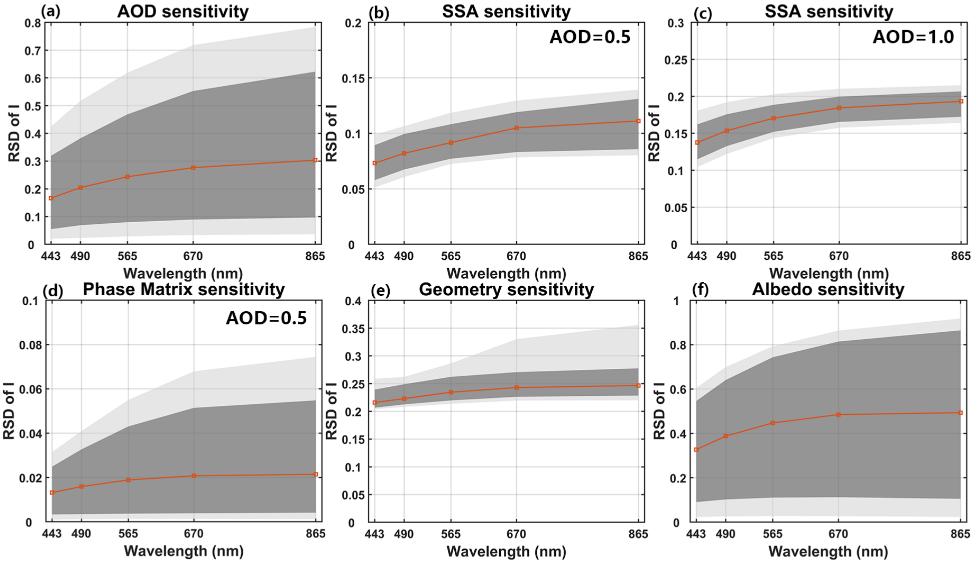

Figure 2. Distributions of relative standard deviation (RSD) of TOA reflectance for aerosol/surface parameters: **(a)** AOD, **(b)** SSA (at AOD = 0.5), **(c)** SSA (at AOD = 1.0), **(d)** Phase Matrix (at AOD = 0.5), **(e)** Geometry, and **(f)** Surface Albedo. The red line indicates the median RSD, the dark grey the central 68 % of the simulations, and light gray the central 90 % of the simulations.

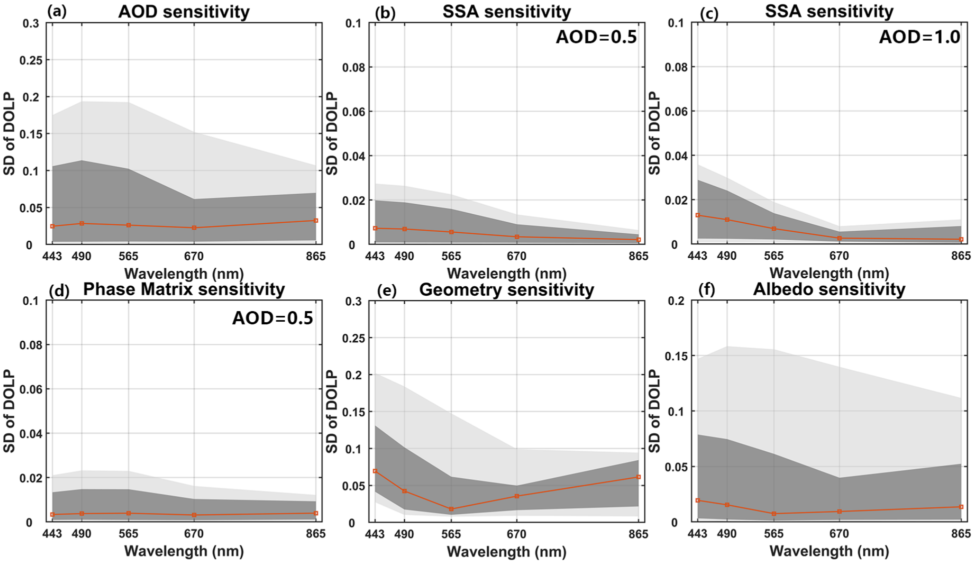

Figure 3. Same as Fig. 2, but for distributions of standard deviation (SD) of DOLP.

DOLP precision of 0.01, with additional constraints on observation angles. Considering that the laboratory calibration uncertainty of DPC's DOLP measurements is already 0.02, and accounting for potential instrument drift after launch, the actual observational uncertainty may exceed 0.04, according to our experiment, it is very difficult to obtain high quality SSA retrieval from DPC observations. However, since DPC's observational uncertainties and required precision are roughly of the same order of magnitude, its measurements can still be used for SSA retrieval to a certain extent, although with reduced precision.

3.2 Retrieval Experiment Using Simulated Data

The accuracy of the retrieved SSA is strongly dependent on aerosol loading, and reliable SSA inversion is generally achieved only when aerosol optical depth is sufficiently high. For this reason, the validation applied an AOD-based screening criterion using AOD_{443} (AOD at 443 nm). Only SSA retrievals with $\text{AOD}_{443} > 0.4$ were retained, consistent with the AERONET fine-mode filtering criterion. This criterion was applied uniformly throughout the analysis, independent of the wavelength at which AOD or SSA was evaluated.

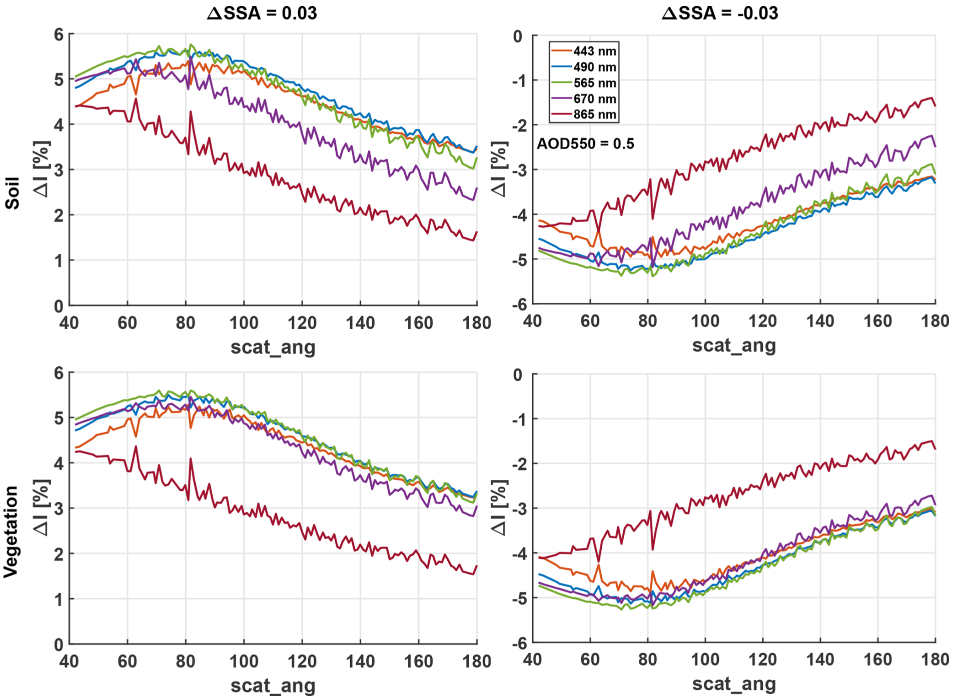

Figure 4. Relative changes in TOA scalar reflectance when the SSA varies by 0.03 (left) and −0.03 (right) under an aerosol loading of $\mathrm{AOD}_{550} = 0.5$ with bare soil (top) and vegetation (bottom) surface type.

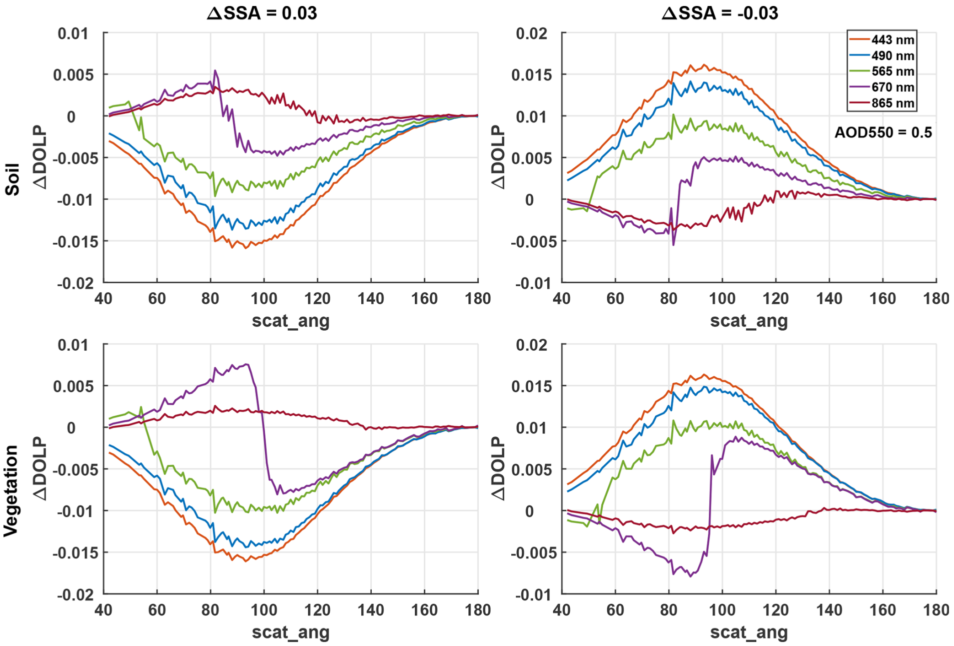

Figure 5. Same as Fig. 4, but for the changes in DOLP.

The retrieval results for the noise-free simulated dataset are presented in Fig. 6. The retrieved AOD and DHR show good agreement with the true values, with points tightly clustered around the 1 : 1 line. Across the four bands, the AOD correlation coefficients are approximately 0.97, while the DHR correlations exceed 0.95 at 443, 565, and 670 nm. Consistent with these patterns, AOD errors remain small, with RMSE ranging from 0.04 to 0.06, bias between −0.004 and 0.013, and MAD ranging from 0.03 to 0.04. DHR errors are of comparable quality, with RMSE close to 0.01, bias between 0.001 and 0.005, and MAD around 0.01. In comparison, SSA retrieval is less accurate even after screening. For cases with $\mathrm{AOD}_{443} > 0.4$, the SSA correlation is approximately 0.6–0.7, and about 55 %–65 % of the retrievals fall within the ±0.03 error envelope (EE). The corresponding SSA RMSE ranges from 0.03 to 0.04, with bias between 0.01 and 0.02 and MAD of approximately 0.03.

When laboratory calibration uncertainties representative of the DPC are introduced, specifically 5 % for radiance and 0.02 for DOLP, retrieval performance degrades as shown in Fig. 7. The degradation is evident for all parameters, with AOD RMSE increasing to 0.06–0.09, bias shifting to 0.02–0.05, and MAD increasing to 0.04–0.07. DHR errors also increase, with RMSE of 0.02–0.04, bias up to 0.01, and MAD around 0.02. The impact is most pronounced for SSA. Under the same $\mathrm{AOD}_{443} > 0.4$ screening, the SSA correlation decreases to approximately 0.4–0.5 and the fraction within the ±0.03 EE drops to about 50 %. The SSA RMSE increases to 0.04–0.05, while bias remains between 0.01 and 0.02 and MAD increases to 0.03–0.04. This behavior is expected because SSA has a relatively limited dynamic range, which makes its inferred variability more susceptible to measurement noise. It should also be noted that the screening uses the retrieved AOD_{443}, rather than the true values. Consequently, the addition of noise perturbs the retrieved AOD and can change the number of SSA retrievals retained after filtering.

Overall, the algorithm yields good retrieval performance for both the noise-free simulations and the simulations with added calibration uncertainties, which supports the effectiveness of the proposed inversion framework. The introduction of noise leads to a systematic degradation in retrieval quality, and the reduction is most evident for SSA, consistent with its limited dynamic range and higher sensitivity to measurement errors. As the uncertainties in actual DPC observations are expected to be larger than the laboratory calibration errors considered here, it is reasonable to anticipate that SSA retrievals from real DPC measurements may exhibit lower accuracy than the simulation-based results, particularly under conditions of moderate aerosol loading.

3.3 Retrieval results on DPC measurements

Validation using the simulated datasets supports the effectiveness of the inversion algorithm. This section further assesses its performance using actual DPC measurements and evaluates the retrievals against AERONET AOD and SSA and MODIS DHR data. The AERONET and MODIS data were interpolated to the DPC wavelengths, and the validation results are presented in Fig. 8.

Overall, retrievals from real DPC observations are consistent with the simulation-based results, with substantially better performance for DHR and AOD than for SSA. The retrieved DHR exhibits moderate to strong correlations with MODIS, with correlation coefficients ranging from 0.75 to 0.93 depending on wavelength, and the agreement generally improves toward longer wavelengths. The associated error magnitudes remain small, with RMSE of approximately 0.03 and MAD of approximately 0.02. The retrieved AOD agrees reasonably well with AERONET, yielding a correlation coefficient of about 0.75, with RMSE of 0.14–0.20, MAD of 0.08–0.13, and bias of 0.02–0.07. This performance is slightly lower than that reported for the operational MODIS AOD products (Levy et al., 2010), but it is comparable in terms of AOD correlation to the DPC retrievals reported by Dong et al. (2024), who obtained a correlation coefficient of 0.76 for AOD at 670 nm. The strong agreement for DHR at longer wavelengths is also consistent with Dong et al. (2024), who reported a DHR correlation coefficient of 0.93, reinforcing that surface reflectance parameters are relatively well constrained by the DPC measurements in this spectral range.

In contrast, SSA retrievals from the present physics-based inversion show substantially weaker agreement with AERONET. For cases with $\mathrm{AOD}_{443} > 0.4$, the retrieved SSA has a correlation coefficient of approximately 0.3, with RMSE of 0.05–0.08, and only about 40 %–45 % of retrievals fall within the ±0.03 EE. This performance differs markedly from the machine-learning based approach of Dong et al. (2024), which reported an SSA correlation coefficient of 0.75 and 73 % of retrievals within the ±0.03 EE. One plausible explanation is that data-driven models can be more tolerant to certain types of observational errors because they implicitly learn empirical mappings from noisy measurements to target variables, provided that the training data adequately represent the noise characteristics. By contrast, the present retrieval relies on explicit radiative transfer consistency between measurements and the forward model, which makes it more sensitive to unmodeled instrument errors and residual calibration uncertainties, particularly for SSA (Zheng et al., 2019). As shown in Sect. 3.1, even under relatively high aerosol loading, an SSA perturbation of 0.03 induces only about a 5 % change in scalar reflectance and a change in DOLP of less than 0.02, implying limited sensitivity. In practice, DPC DOLP uncertainties may exceed 0.04, and although calibration can reduce systematic biases in scalar reflectance, random errors can remain substantial, which further constrains the SSA accuracy. In addition, the reference data used for validation are themselves uncertain. Unlike the simulations, which are compared with a prescribed truth, AERONET SSA has an uncertainty of approximately 0.03, which can further reduce apparent agreement. Applications with real DPC observations may also be affected by additional modeling uncertainties that are absent in the internally consistent simulation framework, although such effects are likely secondary compared with measurement and reference uncertainties.

Nevertheless, satellite-based SSA retrievals remain challenging and typically exhibit relatively low accuracy. The SSA correlation obtained in this study, which is approximately 0.3, is comparable to the regional SSA retrievals from

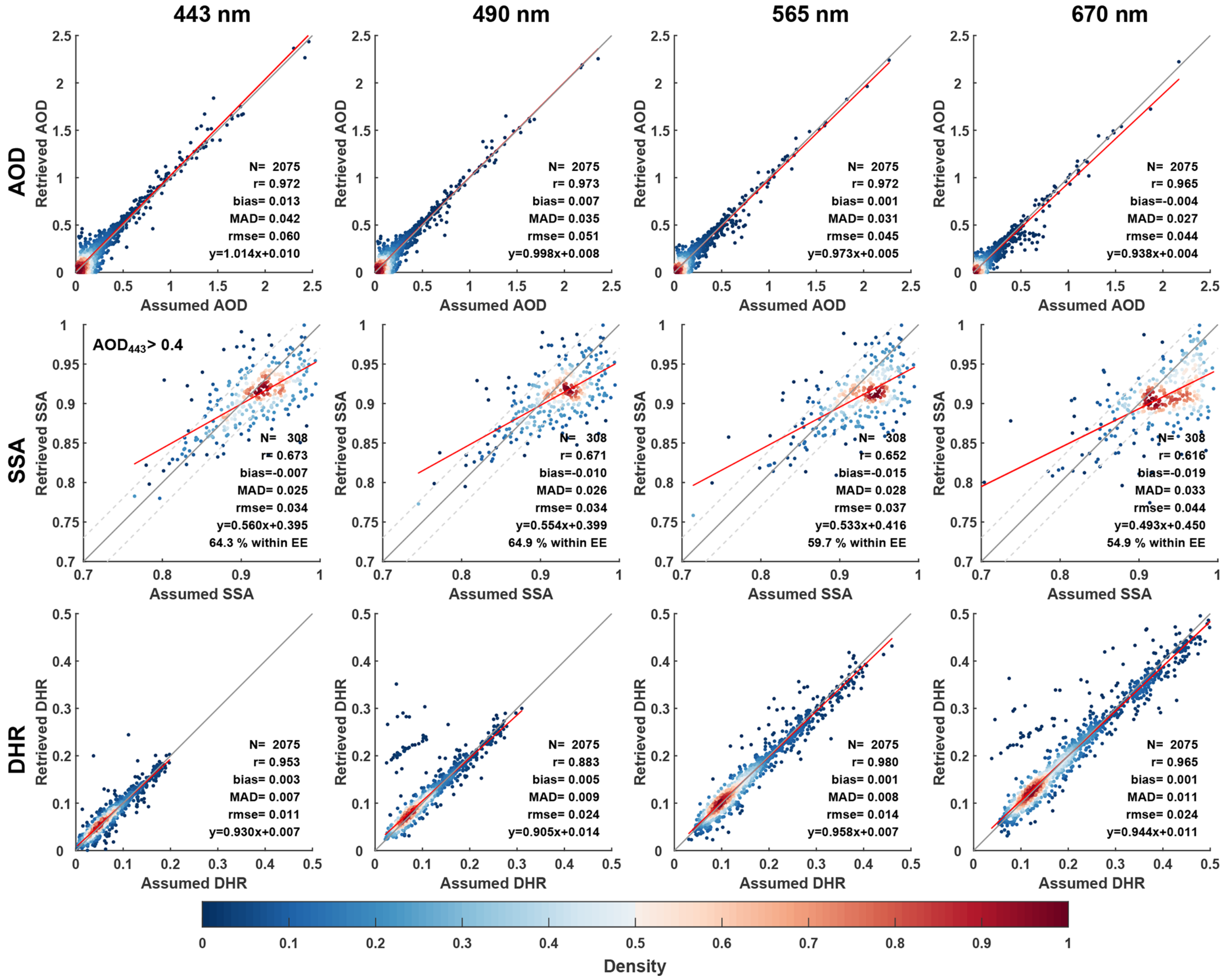

Figure 6. Validation results of AOD (top), SSA(center), and Directional Hemispherical Reflectance (DHR, bottom) at 443, 490, 565, and 670 nm, based on noise-free simulated datasets.

DPC observations reported by Fang et al. (2022). It is also consistent with the reported performance of the POLDER/-GRASP SSA products, which are widely regarded as among the most reliable satellite-based SSA datasets to date and show correlation coefficients of 0.32–0.53 when evaluated against AERONET (Chen et al., 2020). In summary, these comparisons indicate that the proposed algorithm produces AOD and DHR retrievals from DPC observations that are strongly consistent with AERONET and MODIS products, respectively, and that it also provides a reliable, though more limited, capability for SSA retrieval under the applied screening conditions.

3.4 Retrieval Results during Typical Pollution Events

As discussed previously, the retrieval algorithm demonstrates good performance for AOD retrieval and exhibits certain capability for SSA retrieval under pollution conditions. Therefore, it is promising to identify pollution events and characterize major aerosol types using DPC observations. This section examines the retrieval results for a representative biomass burning and dust event respectively as identified from true-color images from MODIS and VIIRS.

Figure 9 presents the true-color image of a fire event in southern Africa on 6 July 2019, along with the retrieved AOD and SSA from DPC observations. The true-color image reveals dense vegetation and numerous smoke plumes, which should be primarily composed of black carbon (BC) and organic carbon (OC) from biomass burning. The AOD retrieval based on DPC observations effectively identifies the spatial distribution of these smoke plumes, highlighting higher aerosol loading in the central, northwestern, and northeastern areas, while lower aerosol concentrations are observed in the southwest and southeast areas. The retrieved AOD also

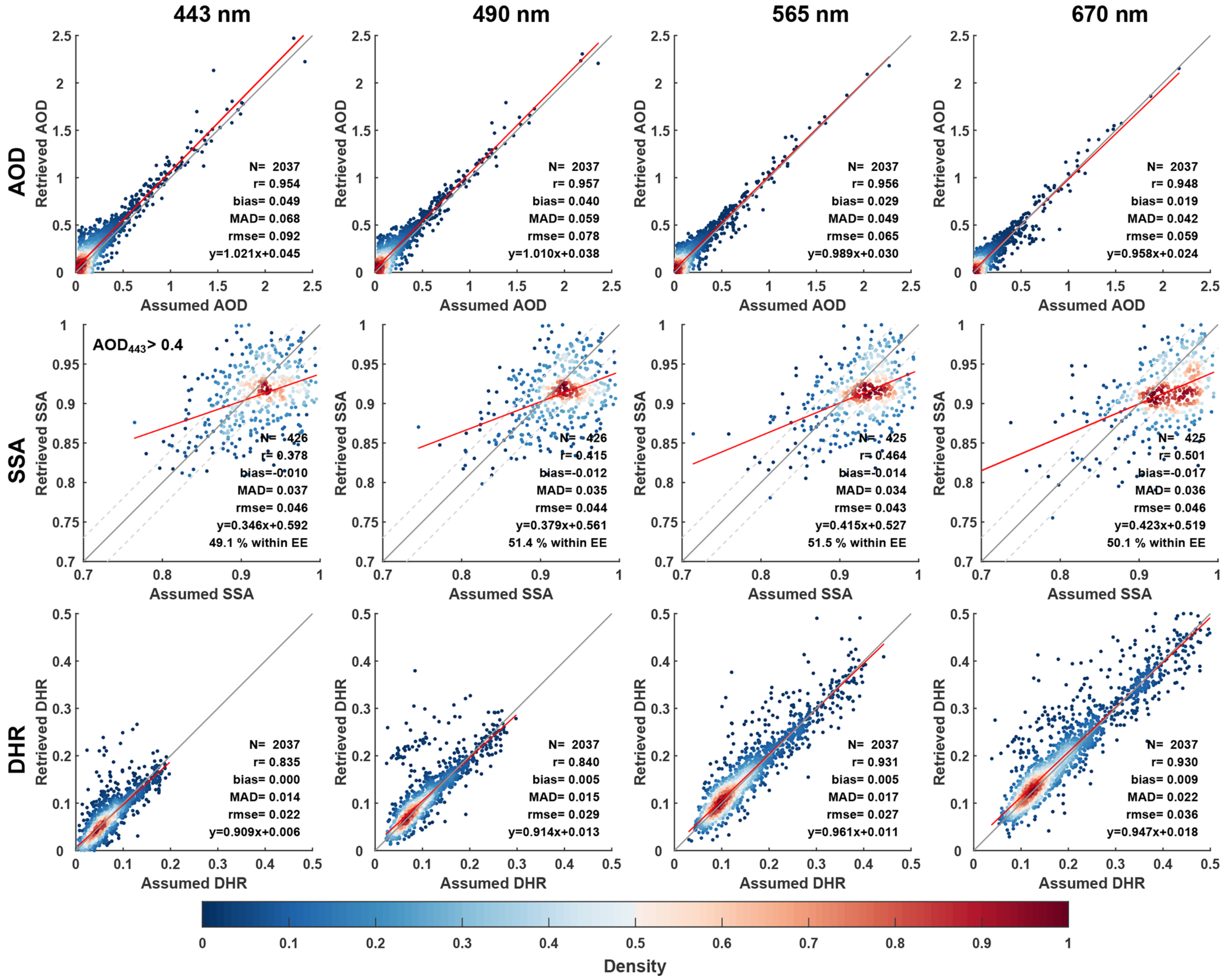

Figure 7. Same as Fig. 6, but with Gaussian noise added to the simulated dataset (5 % for I and 0.02 for DOLP).

reflects the northwest-southeast orientation of these plumes, demonstrating good detection capability for this pollution event. This pattern is also consistent with other satellite AOD products (see the Supplement). The retrieved SSA values are mostly low across the region, typically below 0.9, consistent with the strong absorption properties of biomass burning aerosols, which contain high proportions of BC and/or OC. The relatively higher SSA values in Fig. 9c are mainly located at the edges of the biomass-burning plumes, where AOD is relatively low and the SSA retrieval has larger uncertainty. In these regions, the retrieved SSA (typically around 0.92–0.95) is weakly constrained and therefore more sensitive to the assumed a priori values. Such SSA values suggest moderately absorbing aerosols and may reflect the influence of possible mixing and aging processes near the plume edges, consistent with Kleinman et al. (2020), who reported that near-fire smoke had SSA of ∼ 0.8–0.9, while after ∼ 1–2 h of aging SSA was typically ∼ 0.9 or higher. In regions with higher AOD, the aerosol signal is stronger, leading to better-constrained SSA retrievals with reduced uncertainty. Under these conditions, the retrieved SSA values are systematically lower and exhibit greater spatial consistency, consistent with the presence of strongly absorbing aerosols. Overall, the retrieval results effectively capture the spatial variability in aerosol loading and absorption associated with biomass-burning events.

Figure 10 presents a dust event in northern Africa on 2 October 2019. Coastal pixels are excluded from the retrieval because they cannot be clearly classified as land or ocean, leading to missing values near coastlines. SSA values in low-AOD regions are also screened due to low reliability. The meridional discontinuities in Fig. 10b, c primarily originate from abrupt changes in the observed radiance between successive cross-track scans of DPC, rather than from the re-

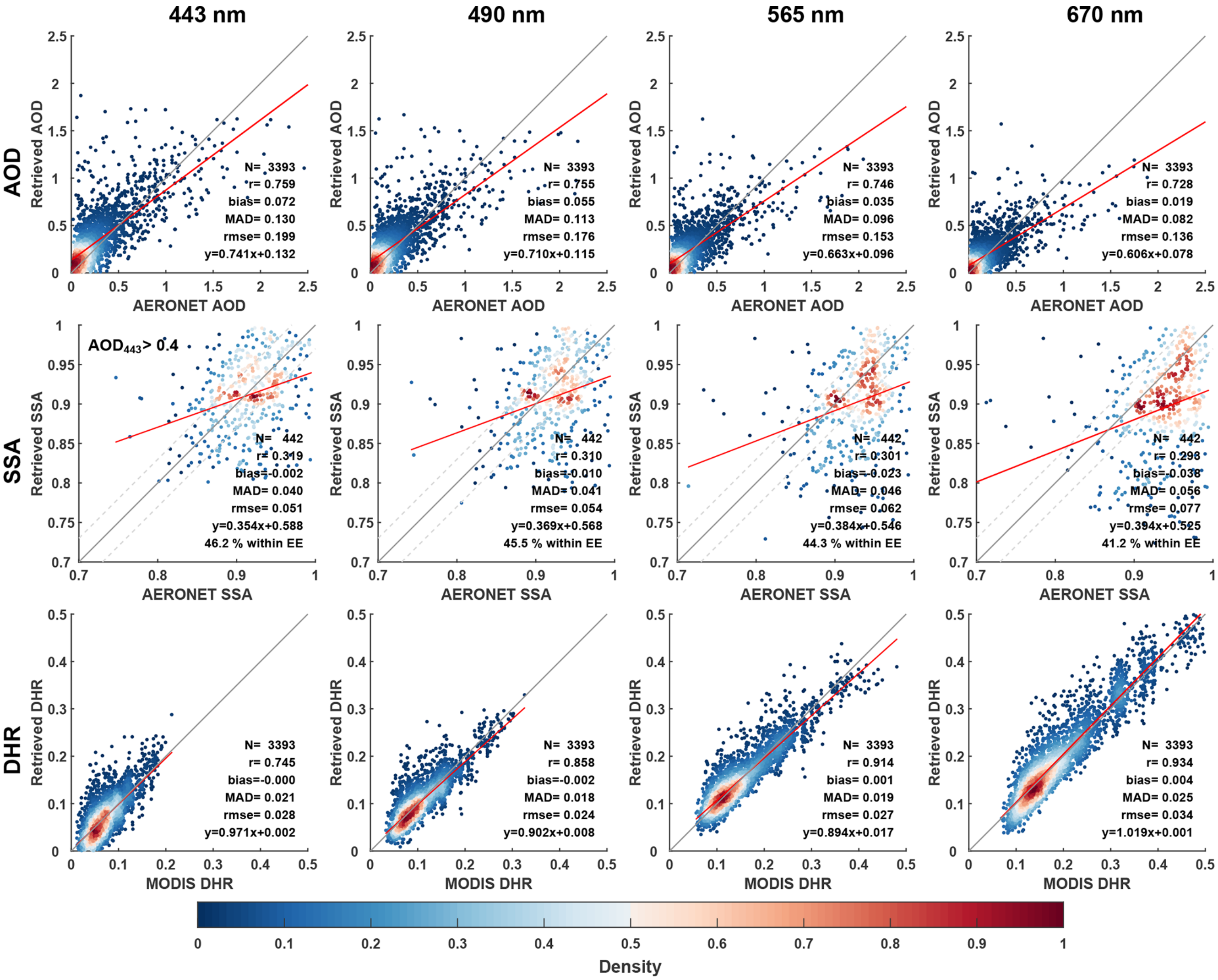

Figure 8. Comparison of retrieved AOD (top) and SSA (center) with AERONET observations, and comparison of retrieved DHR (bottom) with the MODIS product.

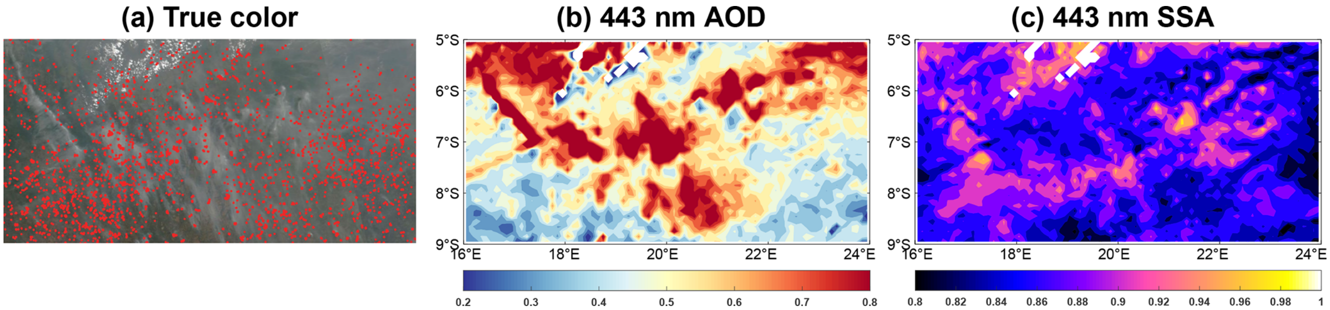

Figure 9. Biomass burning event on 6 July 2019 over southern Africa. **(a)** True-color image from MODIS and VIIRS. **(b)** Retrieved 443 nm AOD from DPC observations. **(c)** Retrieved 443 nm SSA from DPC observations. The true color image covers the same geographic region as panels **(b)** and **(c)**. The true color image is provided by NASA, downloaded from https://worldview.earthdata.nasa.gov/ (last access: 16 June 2025).

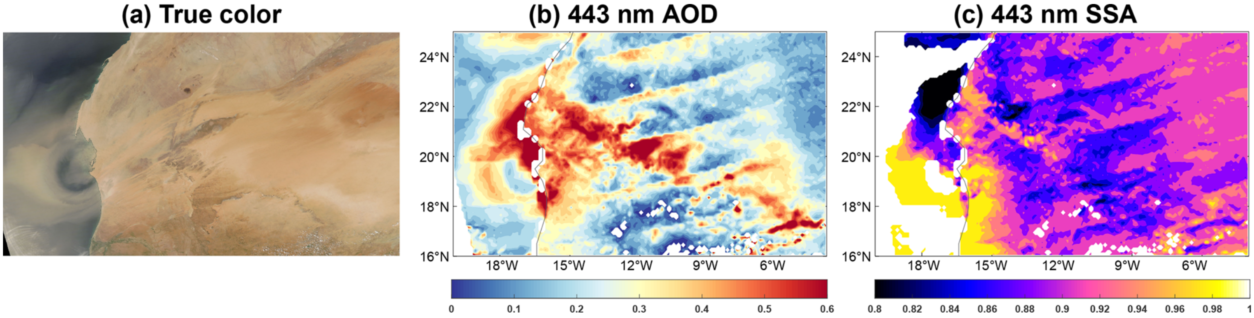

Figure 10. Same as Fig. 9, but with dust event on 2 October 2019 over northern Africa. The true color image is provided by NASA, downloaded from https://worldview.earthdata.nasa.gov/ (last access: 16 June 2025).

trieval algorithm itself. These discontinuities arise when the instrument switches from one cross-track scan to the next, during which the distribution of viewing angle changes. Due to aging of the DPC optical components, the radiometric response exhibits VZA-dependent drifts. Consequently, variations in viewing-angle distribution lead to variations in the magnitude of this drift, leading to radiance inconsistencies between adjacent scans. Although radiometric calibration is applied prior to the retrieval, the VZA-dependent residual errors cannot be completely eliminated. These residual radiometric differences ultimately result in the meridional striping patterns seen in the retrieval results. The true-color image shows intense dust activity in the western part of the region, with some dust transported over the ocean. The retrieved AOD from DPC observations effectively captures the high dust loading in this area, particularly the spiral distribution of aerosols over the ocean, which aligns well with the true-color image and indicates the transport of dust from land to sea. The retrieved SSA values in this region are mostly around 0.92, consistent with typical dust SSA. Thus, the retrieval results also successfully identify this dust event.

In summary, the retrieval algorithm demonstrates good capability for identifying the two pollution events by characterizing the loading and absorbing property of biomass burning and dust aerosols. These results provide valuable references for pollution event detection and aerosol type monitoring.

3.5 Global Retrieval Results

To examine the spatiotemporal variability of aerosol and surface parameters, we further investigate the global and seasonal distribution of retrieved parameters. Figures 11–13 show the global distributions of 443 nm AOD, SSA, and land DHR retrieved from DPC observations for April, July, and October 2019, and January 2020, by gridding the pixel level retrievals to a 0.5° grid resolution. Results for other wavelengths could be found in the Supplement. Overall, the AOD retrievals effectively capture major aerosol source regions (Fig. 11), the spatiotemporal distribution of SSA aligns with regional emission characteristics (Fig. 12), and DHR closely matches local surface types (Fig. 13). The patterns of AOD, SSA, and DHR are highly consistent with other satellite products such as MODIS, OMI, and POLDER (Chen et al., 2020; Heald et al., 2014; Schutgens et al., 2021), and are also in line with previous studies applying DPC observations (Dong et al., 2024).

Specifically, high AOD values are concentrated in the majority of aerosol source regions such as East Asia, South Asia, Africa, the Arabian Peninsula, and northern South America (Fig. 11). Despite using different surface assumptions for land and ocean, the AOD spatial distribution exhibits strong continuity, including the westward transport of Sahara dust in the northern Africa (Engelstaedter et al., 2006) and the spread of aerosols from land to the ocean in pre-monsoon over South Asia (Satheesh and Srinivasan, 2002). The distributions of SSA (Fig. 12) reflect the scattering and absorption properties of aerosols in different regions, highlighting aerosol composition features. Low SSA values are retrieved in Central Asia, Africa, the Arabian Peninsula, central Australia, and western North America, indicating stronger aerosol absorption in these areas. Among these, Central Asia, northern Africa, and the Arabian Peninsula are major dust source regions (Ginoux et al., 2012; Habib et al., 2019), where low SSA is primarily associated with dust emissions. Biomass burning regions in southern Africa, northern South America, western North America, and Australia, also exhibit low SSA values, which are mainly associated with BC and/or OC emissions (Eck et al., 2023; Iglesias et al., 2022; Mallet et al., 2024; Pan et al., 2020; Yang et al., 2021). In contrast, Europe and eastern North America exhibit higher SSA values due to dominant anthropogenic emissions of scattering-type fine particles (Li et al., 2016; Ramanathan et al., 2001; Wei et al., 2024; Zhang et al., 2025a).

The spatial distribution of DHR (Fig. 13) aligns well with local surface types (Yang et al., 2017). Regions such as South America, southern Africa, Europe, Siberia, and eastern North America show lower DHR in summer, reflecting dense vegetation coverage in this season. Conversely, Central Asia, West Africa, and the Arabian Peninsula exhibit higher DHR due to desert surfaces with higher reflectivity. Some regions in western North America and central Australia also exhibit

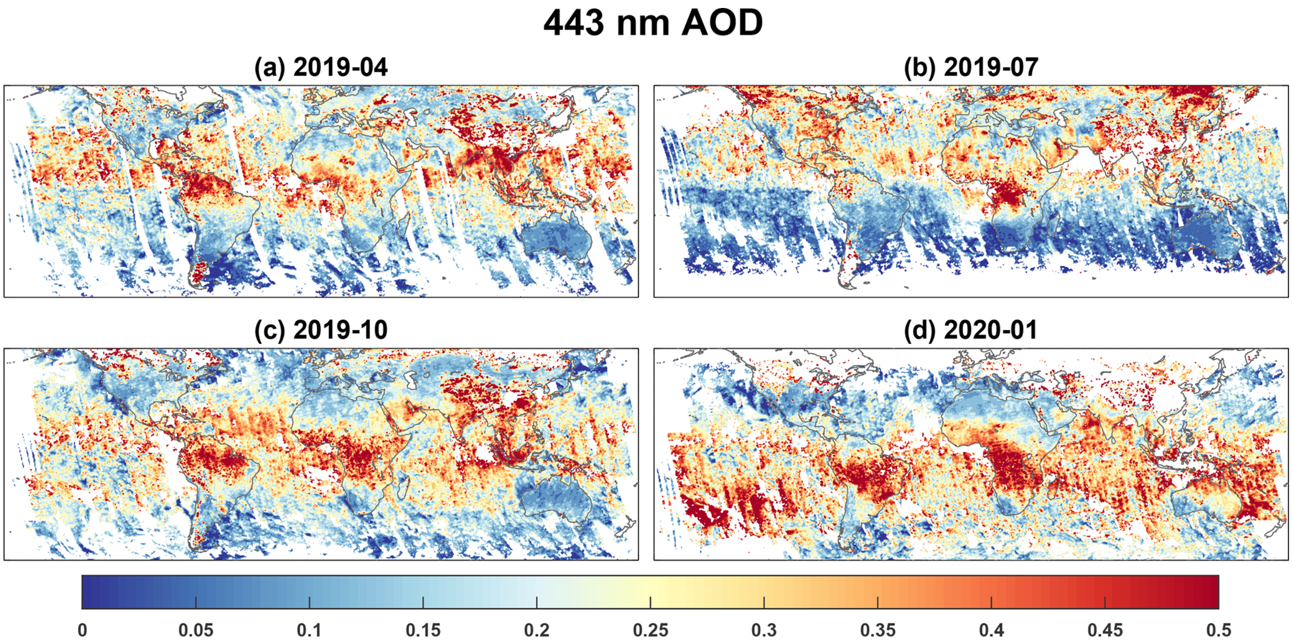

Figure 11. Global 443 nm AOD retrieved from DPC observations.

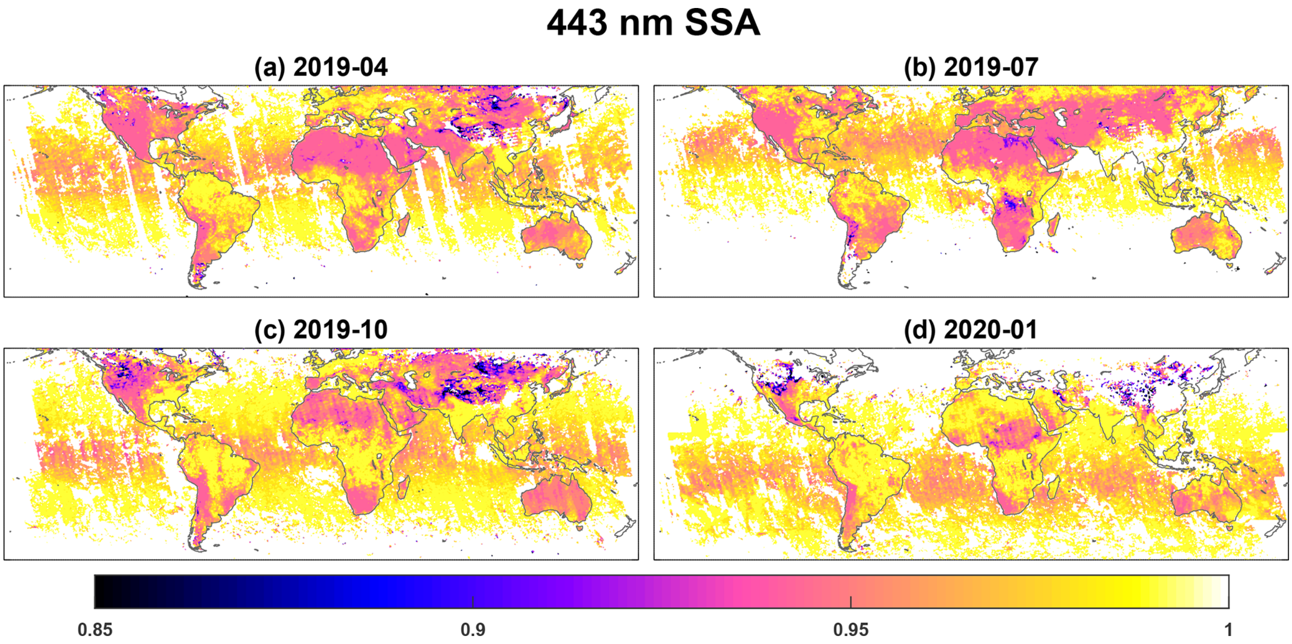

Figure 12. Same as Fig. 11, but for 443 nm SSA.

high DHR values, consistent with the drier soil associated with arid climate condition there.

Additionally, the global distributions of AOD, SSA, and DHR across different months effectively capture the seasonal variations in aerosol and surface properties. For instance, high-latitude regions in the Northern Hemisphere exhibit higher DHR in winter than that in summer, reflecting drier conditions and reduced vegetation coverage during winter. In West Africa, intense dust activity during the summer months corresponds to higher AOD (Fig. 11a, b), while AOD is relatively lower in other seasons (Fig. 11c, d). Biomass burning in southern Africa primarily occurs during dry seasons (Mallet et al., 2024; Pan et al., 2020), such as in July when lower SSA values are derived from DPC observations (Fig. 12b). The elevated AOD in northern South America in October (Fig. 11c) is linked to active wildfires

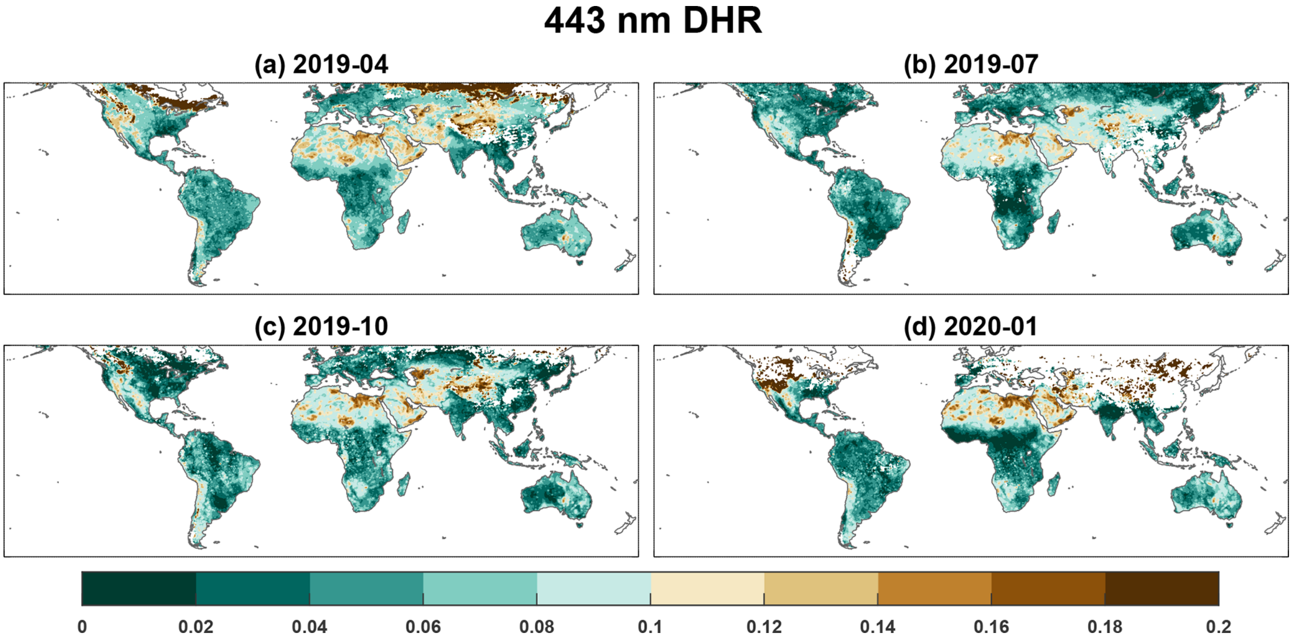

Figure 13. Same as Fig. 11, but for 443 nm DHR.

during that season (Pan et al., 2020). Notably, while Australia generally exhibits low AOD, significantly higher AOD was observed in January 2020, associated with strong wildfires that began in late 2019. Figure 11d shows the eastward transport of aerosols from Australia, forming a distinct high-AOD band over the Southern Oceans, where SSA also shows lower values. The anomalously high AOD over the Southern Ocean in January 2020 reaches values of up to 0.5 in some regions, consistent with independent data sources (e.g., MODIS AOD, see Supplement). Our DPC retrieval results successfully capture these extreme events.

4 Discussion and Conclusion

Satellite-based retrieval of comprehensive aerosol and surface properties remains a challenging work due to limitations in observational information and the lack of constraints of unknown parameters. Multi-angle polarimetric observations represent a great advancement in this regard, as their great information content enables the retrieval of multiple parameters, including aerosol absorption and surface reflectance (Dubovik et al., 2019). While some studies using DPC observations have demonstrated robust AOD retrievals (Ge et al., 2022; Jin et al., 2022; Wang et al., 2021), progress in SSA retrieval was still quite limited, with no operational global SSA products currently available from DPC observations.

This study developed a numerical algorithm to retrieve global AOD, SSA, and DHR based on DPC observations, achieving results with reasonable accuracy. Our work provides insights into the potential of multi-angle polarimetric observations for the retrieval of aerosol and surface properties, deriving high quality AOD and DHR retrieval and reliable SSA retrieval. The ability to reliably retrieve SSA from space has profound implications for more accurate assessment of aerosol radiative effects and environmental impacts, representing an important advancement in atmospheric remote sensing capabilities. The sensitivity experiments and global-scale results presented here also offer insights into future development of spaceborne multi-angle polarimetric sensors.

The sensitivity analysis of scalar and polarimetric observations to SSA in this work demonstrates that accurate SSA retrieval with an uncertainty of 0.03 requires DOLP observation uncertainties below 0.01 even with optimally designed viewing geometries. The laboratory calibration uncertainty of DPC's DOLP measurements is roughly on par with this requirement (Li et al., 2018), theoretically enabling SSA retrieval. The performance of our algorithm on simulated data further indicates that, within DPC's designed precision, SSA retrieval is feasible, with correlation coefficients between retrieved and "true" 443 nm SSA reaching 0.8 when AOD exceeds 0.5. However, retrieval based on multi-angle polarization observations is highly sensitive to measurement uncertainties (Zheng et al., 2019). Since launch, DPC's optical components have aged, significantly increasing scalar and polarimetric uncertainties (potentially exceeding 10 % for scalar reflectance and 0.04 for DOLP) without effective evaluation or correction methods (Qie et al., 2021; Zhu et al., 2022), which partially explains the difficulty in achieving high-precision SSA retrieval from DPC measurements. In our global validation against AERONET observations, the SSA correlation coefficient reaches approximately 0.38

when 443 nm AOD $>$ 0.4, comparable to the regional retrieval results reported by Fang et al. (2022). The POLDER/-GRASP SSA product shows correlation coefficients of 0.32–0.54 for its best-performing 670 nm band when AOD $>$ 0.3 (Chen et al., 2020), also similar to our SSA validation results.

Furthermore, this study derived regional and global distributions of AOD and SSA from DPC observations, along with land surface DHR. Regional results effectively identify pollution events and characterize major aerosol types. The global AOD also reveals major aerosol source regions, while the SSA distribution reflects regional aerosol composition characteristics. The spatial pattern of DHR shows good agreement with local surface types.

In sum, our retrieval results demonstrate the potential of DPC observations for comprehensive aerosol and surface monitoring, despite current limitations in SSA retrieval accuracy. Nonetheless, to an accuracy level of AOD and SSA that meet the requirement of aerosol forcing estimation which requires the uncertainty of SSA to be within 0.03 and that of AOD to be within 10 % (Mishchenko et al., 2004; Loeb and Su, 2010; Zhang et al., 2022), significantly higher quality of scalar and DOLP measurements are needed than the current DPC sensor. The information provided by DPC should thus be considered more qualitative than quantitative. Future improvements in sensor design, calibration, as well as retrieval algorithms may further enhance the precision of aerosol retrievals and provide more quantitative products.

Code and data availability. The AERONET data are available at https://aeronet.gsfc.nasa.gov (last access: 15 October 2025). The MODIS data are available at https://ladsweb.modaps.eosdis.nasa.gov (last access: 15 October 2025). The ERA5 data are available at https://cds.climate.copernicus.eu (last access: 15 October 2025). The salinity data are available at https://ncss.hycom.org/thredds/catalog.html (last access: 15 October 2025). The gridded global retrieval results are available at https://doi.org/10.18170/DVN/YMRDFC (Zhang, 2026). Other data and codes will be made available on request.

Supplement. The supplement related to this article is available online at https://doi.org/10.5194/amt-19-2555-2026-supplement.

Author contributions. JL designed the research. ZZ implemented the research. ZZ and JL wrote the initial draft. YD and CZ helped preprocess the data. YD, CZ, QL, and LG helped collect data and provided guidance in improving the draft.

Competing interests. The contact author has declared that none of the authors has any competing interests.

Disclaimer. Publisher's note: Copernicus Publications remains neutral with regard to jurisdictional claims made in the text, published maps, institutional affiliations, or any other geographical representation in this paper. The authors bear the ultimate responsibility for providing appropriate place names. Views expressed in the text are those of the authors and do not necessarily reflect the views of the publisher.

Acknowledgements. We gratefully thank the Chinese National Space Administration Earth Observation and Data Center for providing the DPC/GF-5 data. We appreciate the AEROENT team for supporting the sunphotometers network (https://aeronet.gsfc.nasa.gov/, last access: 15 October 2025). We also acknowledge NASA for providing MODIS data (https://ladsweb.modaps.eosdis.nasa.gov, last access: 15 October 2025) and the true-color images used in the article (https://worldview.earthdata.nasa.gov/, last access: 16 June 2025). This work is funded by National Natural Science Foundation of China Grant No. 42425503, and National Key Research and Development Program of China (Grant 2023YFF0805401).

Financial support. This research has been supported by the National Natural Science Foundation of China (grant no. 42425503) and the National Key Research and Development Program of China (grant no. 2023YFF0805401).

Review statement. This paper was edited by Alexander Kokhanovsky and reviewed by five anonymous referees.

References

Albrecht, B. A.: Aerosols, Cloud Microphysics, and Fractional Cloudiness, Science, 245, 1227–1230, https://doi.org/10.1126/science.245.4923.1227, 1989.

Chen, C., Dubovik, O., Fuertes, D., Litvinov, P., Lapyonok, T., Lopatin, A., Ducos, F., Derimian, Y., Herman, M., Tanré, D., Remer, L. A., Lyapustin, A., Sayer, A. M., Levy, R. C., Hsu, N. C., Descloitres, J., Li, L., Torres, B., Karol, Y., Herrera, M., Herreras, M., Aspetsberger, M., Wanzenboeck, M., Bindreiter, L., Marth, D., Hangler, A., and Federspiel, C.: Validation of GRASP algorithm product from POLDER/PARASOL data and assessment of multi-angular polarimetry potential for aerosol monitoring, Earth Syst. Sci. Data, 12, 3573–3620, https://doi.org/10.5194/essd-12-3573-2020, 2020.

Cummings, J. A. and Smedstad, O. M.: Variational Data Assimilation for the Global Ocean, Springer Berlin Heidelberg, 303–343, https://doi.org/10.1007/978-3-642-35088-7_13, ISBN 9783642350887, 2013.

Dai, G., Wu, S., Long, W., Liu, J., Xie, Y., Sun, K., Meng, F., Song, X., Huang, Z., and Chen, W.: Aerosol and cloud data processing and optical property retrieval algorithms for the spaceborne ACDL/DQ-1, Atmos. Meas. Tech., 17, 1879–1890, https://doi.org/10.5194/amt-17-1879-2024, 2024.

Diner, D. J., Beckert, J. C., Reilly, T. H., Bruegge, C. J., Conel, J. E., Kahn, R. A., Martonchik, J. V., Ackerman, T. P., Davies, R., and Gerstl, S. A.: Multi-angle Imaging SpectroRadiometer (MISR) instrument description and experiment overview, IEEE T. Geosci. Remote, 36, 1072–1087, 1998.

Dong, Y., Li, J., Zhang, Z., Zheng, Y., Zhang, C., and Li, Z.: Machine Learning-Based Retrieval of Aerosol and Surface Properties Over Land From the Gaofen-5 Directional Polarimetric Camera Measurements, IEEE T. Geosci. Remote, 62, 1–15, https://doi.org/10.1109/tgrs.2024.3419169, 2024.

Dubovik, O. and King, M. D.: A flexible inversion algorithm for retrieval of aerosol optical properties from Sun and sky radiance measurements, J. Geophys. Res.-Atmos., 105, 20673–20696, https://doi.org/10.1029/2000jd900282, 2000.

Dubovik, O., Smirnov, A., Holben, B. N., King, M. D., Kaufman, Y. J., Eck, T. F., and Slutsker, I.: Accuracy assessments of aerosol optical properties retrieved from Aerosol Robotic Network (AERONET) Sun and sky radiance measurements, J. Geophys. Res.-Atmos., 105, 9791–9806, https://doi.org/10.1029/2000jd900040, 2000.

Dubovik, O., Herman, M., Holdak, A., Lapyonok, T., Tanré, D., Deuzé, J. L., Ducos, F., Sinyuk, A., and Lopatin, A.: Statistically optimized inversion algorithm for enhanced retrieval of aerosol properties from spectral multi-angle polarimetric satellite observations, Atmos. Meas. Tech., 4, 975–1018, https://doi.org/10.5194/amt-4-975-2011, 2011.

Dubovik, O., Li, Z., Mishchenko, M. I., Tanré, D., Karol, Y., Bojkov, B., Cairns, B., Diner, D. J., Espinosa, W. R., Goloub, P., Gu, X., Hasekamp, O., Hong, J., Hou, W., Knobelspiesse, K. D., Landgraf, J., Li, L., Litvinov, P., Liu, Y., Lopatin, A., Marbach, T., Maring, H., Martins, V., Meijer, Y., Milinevsky, G., Mukai, S., Parol, F., Qiao, Y., Remer, L., Rietjens, J., Sano, I., Stammes, P., Stamnes, S., Sun, X., Tabary, P., Travis, L. D., Waquet, F., Xu, F., Yan, C., and Yin, D.: Polarimetric remote sensing of atmospheric aerosols: Instruments, methodologies, results, and perspectives, J. Quant. Spectrosc. Ra., 224, 474–511, https://doi.org/10.1016/j.jqsrt.2018.11.024, 2019.

Eck, T. F., Holben, B. N., Reid, J. S., Sinyuk, A., Giles, D. M., Arola, A., Slutsker, I., Schafer, J. S., Sorokin, M. G., Smirnov, A., LaRosa, A. D., Kraft, J., Reid, E. A., O'Neill, N. T., Welton, E., and Menendez, A. R.: The extreme forest fires in California/Oregon in 2020: Aerosol optical and physical properties and comparisons of aged versus fresh smoke, Atmos. Environ., 305, 119798, https://doi.org/10.1016/j.atmosenv.2023.119798, 2023.

Engelstaedter, S., Tegen, I., and Washington, R.: North African dust emissions and transport, Earth-Sci. Rev., 79, 73–100, https://doi.org/10.1016/j.earscirev.2006.06.004, 2006.

Fang, L., Hasekamp, O., Fu, G., Gong, W., Wang, S., Wang, W., Han, Q., and Tang, S.: Retrieval of Aerosol Optical Properties over Land Using an Optimized Retrieval Algorithm Based on the Directional Polarimetric Camera, Remote Sensing, 14, 4571, https://doi.org/10.3390/rs14184571, 2022.

GCOS: The Global Observing System For Climate: Implementation Needs, GCOS-200 (GOOS-214), WMO, Geneva, 341 pp., https://library.wmo.int/records/item/55469-the-global-observing-system-for-climate (last access: 13 April 2026), 2016.

Ge, B., Li, Z., Chen, C., Hou, W., Xie, Y., Zhu, S., Qie, L., Zhang, Y., Li, K., and Xu, H.: An Improved Aerosol Optical Depth Retrieval Algorithm for Multiangle Directional Polarimetric Camera (DPC), Remote Sensing, 14, 4045, https://doi.org/10.3390/rs14164045, 2022.

Giles, D. M., Sinyuk, A., Sorokin, M. G., Schafer, J. S., Smirnov, A., Slutsker, I., Eck, T. F., Holben, B. N., Lewis, J. R., Campbell, J. R., Welton, E. J., Korkin, S. V., and Lyapustin, A. I.: Advancements in the Aerosol Robotic Network (AERONET) Version 3 database – automated near-real-time quality control algorithm with improved cloud screening for Sun photometer aerosol optical depth (AOD) measurements, Atmos. Meas. Tech., 12, 169–209, https://doi.org/10.5194/amt-12-169-2019, 2019.

Ginoux, P., Prospero, J. M., Gill, T. E., Hsu, N. C., and Zhao, M.: Global-scale attribution of anthropogenic and natural dust sources and their emission rates based on MODIS Deep Blue aerosol products, Rev. Geophys., 50, https://doi.org/10.1029/2012rg000388, 2012.

Habib, A., Chen, B., Khalid, B., Tan, S., Che, H., Mahmood, T., Shi, G., and Butt, M. T.: Estimation and inter-comparison of dust aerosols based on MODIS, MISR and AERONET retrievals over Asian desert regions, J. Environ. Sci., 76, 154–166, https://doi.org/10.1016/j.jes.2018.04.019, 2019.

Hasekamp, O. P., Litvinov, P., and Butz, A.: Aerosol properties over the ocean from PARASOL multiangle photopolarimetric measurements, J. Geophys. Res.-Atmos., 116, D14204, https://doi.org/10.1029/2010JD015469, 2011.

Hasekamp, O., Litvinov, P., Fu, G., Chen, C., and Dubovik, O.: Algorithm evaluation for polarimetric remote sensing of atmospheric aerosols, Atmos. Meas. Tech., 17, 1497–1525, https://doi.org/10.5194/amt-17-1497-2024, 2024.

Heald, C. L., Ridley, D. A., Kroll, J. H., Barrett, S. R. H., Cady-Pereira, K. E., Alvarado, M. J., and Holmes, C. D.: Contrasting the direct radiative effect and direct radiative forcing of aerosols, Atmos. Chem. Phys., 14, 5513–5527, https://doi.org/10.5194/acp-14-5513-2014, 2014.

Hersbach, H., Bell, B., Berrisford, P., Hirahara, S., Horányi, A., Muñoz-Sabater, J., Nicolas, J., Peubey, C., Radu, R., Schepers, D., Simmons, A., Soci, C., Abdalla, S., Abellan, X., Balsamo, G., Bechtold, P., Biavati, G., Bidlot, J., Bonavita, M., De Chiara, G., Dahlgren, P., Dee, D., Diamantakis, M., Dragani, R., Flemming, J., Forbes, R., Fuentes, M., Geer, A., Haimberger, L., Healy, S., Hogan, R. J., Hólm, E., Janisková, M., Keeley, S., Laloyaux, P., Lopez, P., Lupu, C., Radnoti, G., de Rosnay, P., Rozum, I., Vamborg, F., Villaume, S., and Thépaut, J.: The ERA5 global reanalysis, Q. J. Roy. Meteor. Soc., 146, 1999–2049, https://doi.org/10.1002/qj.3803, 2020.

Holben, B. N., Eck, T. F., Slutsker, I., Tanré, D., Buis, J. P., Setzer, A., Vermote, E., Reagan, J. A., Kaufman, Y. J., Nakajima, T., Lavenu, F., Jankowiak, I., and Smirnov, A.: AERONET – A Federated Instrument Network and Data Archive for Aerosol Characterization, Remote Sens. Environ., 66, 1–16, https://doi.org/10.1016/S0034-4257(98)00031-5, 1998.

Iglesias, V., Balch, J. K., and Travis, W. R.: U.S. fires became larger, more frequent, and more widespread in the 2000s, Science Advances, 8, https://doi.org/10.1126/sciadv.abc0020, 2022.

Ji, Z., Li, Z., Zhang, Z., Fu, G., Hasekamp, O., Fan, C., Liu, Q., and de Leeuw, G.: Retrieval of Aerosol Properties Over the Ocean Using Data From the Second-Generation Directional Polarization Camera (DPC-2) Onboard the GF-5(02) Satellite, J. Geophys. Res.-Atmos., 130, https://doi.org/10.1029/2025jd043908, 2025.

Jin, S., Ma, Y., Chen, C., Dubovik, O., Hong, J., Liu, B., and Gong, W.: Performance evaluation for retrieving aerosol optical depth from the Directional Polarimetric Camera (DPC) based on the GRASP algorithm, Atmos. Meas. Tech., 15, 4323–4337, https://doi.org/10.5194/amt-15-4323-2022, 2022.

Jin, S., Ma, Y., Wang, Z., Hong, J., Chen, F., Ti, R., Chen, C., Liu, Z., Zhai, S., and Gong, W.: Retrievals and performance assessment of global marine aerosol optical properties from DPC/-GRASP, Journal of Atmospheric and Environmental Optics, 19, 680–697, 2024.

Kleinman, L. I., Sedlacek III, A. J., Adachi, K., Buseck, P. R., Collier, S., Dubey, M. K., Hodshire, A. L., Lewis, E., Onasch, T. B., Pierce, J. R., Shilling, J., Springston, S. R., Wang, J., Zhang, Q., Zhou, S., and Yokelson, R. J.: Rapid evolution of aerosol particles and their optical properties downwind of wildfires in the western US, Atmos. Chem. Phys., 20, 13319–13341, https://doi.org/10.5194/acp-20-13319-2020, 2020.

Levy, R. C., Remer, L. A., and Dubovik, O.: Global aerosol optical properties and application to Moderate Resolution Imaging Spectroradiometer aerosol retrieval over land, J. Geophys. Res.-Atmos., 112, D13210, https://doi.org/10.1029/2006jd007815, 2007a.

Levy, R. C., Remer, L. A., Mattoo, S., Vermote, E. F., and Kaufman, Y. J.: Second-generation operational algorithm: Retrieval of aerosol properties over land from inversion of Moderate Resolution Imaging Spectroradiometer spectral reflectance, J. Geophys. Res.-Atmos., 112, D13211, https://doi.org/10.1029/2006jd007811, 2007b.

Levy, R. C., Remer, L. A., Kleidman, R. G., Mattoo, S., Ichoku, C., Kahn, R., and Eck, T. F.: Global evaluation of the Collection 5 MODIS dark-target aerosol products over land, Atmos. Chem. Phys., 10, 10399–10420, https://doi.org/10.5194/acp-10-10399-2010, 2010.

Levy, R. C., Mattoo, S., Munchak, L. A., Remer, L. A., Sayer, A. M., Patadia, F., and Hsu, N. C.: The Collection 6 MODIS aerosol products over land and ocean, Atmos. Meas. Tech., 6, 2989–3034, https://doi.org/10.5194/amt-6-2989-2013, 2013.

Li, J., Li, X., Carlson, B. E., Kahn, R. A., Lacis, A. A., Dubovik, O., and Nakajima, T.: Reducing multisensor satellite monthly mean aerosol optical depth uncertainty: 1. Objective assessment of current AERONET locations, J. Geophys. Res.-Atmos., 121, https://doi.org/10.1002/2016jd025469, 2016.

Li, J., Carlson, B. E., Yung, Y. L., Lv, D., Hansen, J., Penner, J. E., Liao, H., Ramaswamy, V., Kahn, R. A., Zhang, P., Dubovik, O., Ding, A., Lacis, A. A., Zhang, L., and Dong, Y.: Scattering and absorbing aerosols in the climate system, Nature Reviews Earth & Environment, 3, 363–379, https://doi.org/10.1038/s43017-022-00296-7, 2022a.

Li, L., Dubovik, O., Derimian, Y., Schuster, G. L., Lapyonok, T., Litvinov, P., Ducos, F., Fuertes, D., Chen, C., Li, Z., Lopatin, A., Torres, B., and Che, H.: Retrieval of aerosol components directly from satellite and ground-based measurements, Atmos. Chem. Phys., 19, 13409–13443, https://doi.org/10.5194/acp-19-13409-2019, 2019.

Li, Z., Hou, W., Hong, J., Zheng, F., Luo, D., Wang, J., Gu, X., and Qiao, Y.: Directional Polarimetric Camera (DPC): Monitoring aerosol spectral optical properties over land from satellite observation, J. Quant. Spectrosc. Ra., 218, 21–37, https://doi.org/10.1016/j.jqsrt.2018.07.003, 2018.

Li, Z., Hou, W., Hong, J., Fan, C., Wei, Y., Liu, Z., Lei, X., Qiao, Y., Hasekamp, O. P., Fu, G., Wang, J., Dubovik, O., Qie, L., Zhang, Y., Xu, H., Xie, Y., Song, M., Zou, P., Luo, D., Wang, Y., and Tu, B.: The polarization crossfire (PCF) sensor suite focusing on satellite remote sensing of fine particulate matter $PM_{2.5}$ from space, J. Quant. Spectrosc. Ra., 286, 108217, https://doi.org/10.1016/j.jqsrt.2022.108217, 2022b.

Litvinov, P., Hasekamp, O., and Cairns, B.: Models for surface reflection of radiance and polarized radiance: Comparison with airborne multi-angle photopolarimetric measurements and implications for modeling top-of-atmosphere measurements, Remote Sens. Environ., 115, 781–792, https://doi.org/10.1016/j.rse.2010.11.005, 2011.

Liu, C., Gao, M., Hu, Q., Brasseur, G. P., and Carmichael, G. R.: Stereoscopic Monitoring: A Promising Strategy to Advance Diagnostic and Prediction of Air Pollution, B. Am. Meteorol. Soc., 102, E730–E737, https://doi.org/10.1175/bams-d-20-0217.1, 2021.

Loeb, N. G. and Su, W.: Direct Aerosol Radiative Forcing Uncertainty Based on a Radiative Perturbation Analysis, J. Climate, 23, 5288–5293, https://doi.org/10.1175/2010jcli3543.1, 2010.

Maignan, F., Bréon, F.-M., Fédèle, E., and Bouvier, M.: Polarized reflectances of natural surfaces: Spaceborne measurements and analytical modeling, Remote Sens. Environ., 113, 2642–2650, https://doi.org/10.1016/j.rse.2009.07.022, 2009.

Mallet, M., Voldoire, A., Solmon, F., Nabat, P., Drugé, T., and Roehrig, R.: Impact of biomass burning aerosols (BBA) on the tropical African climate in an ocean–atmosphere–aerosol coupled climate model, Atmos. Chem. Phys., 24, 12509–12535, https://doi.org/10.5194/acp-24-12509-2024, 2024.

Mishchenko, M., Cairns, B., Kopp, G., Maring, H., Fafaul, B., Knobelspiesse, K., and Chowdhary, J.: Accurate monitoring of terrestrial aerosols and total solar irradiance: The NASA Glory mission, in: 2010 IEEE International Geoscience and Remote Sensing Symposium, Honolulu, HI, USA, 25–30 July 2010, IEEE, 758–760, https://doi.org/10.1109/igarss.2010.5652996, 2010.

Mishchenko, M. I. and Travis, L. D.: Light scattering by polydisperse, rotationally symmetric nonspherical particles: Linear polarization, J. Quant. Spectrosc. Ra., 51, 759–778, https://doi.org/10.1016/0022-4073(94)90130-9, 1994.

Mishchenko, M. I., Cairns, B., Hansen, J. E., Travis, L. D., Burg, R., Kaufman, Y. J., Vanderlei Martins, J., and Shettle, E. P.: Monitoring of aerosol forcing of climate from space: analysis of measurement requirements, J. Quant. Spectrosc. Ra., 88, 149–161, https://doi.org/10.1016/j.jqsrt.2004.03.030, 2004.

Mishchenko, M. I., Geogdzhayev, I. V., Rossow, W. B., Cairns, B., Carlson, B. E., Lacis, A. A., Liu, L., and Travis, L. D.: Long-Term Satellite Record Reveals Likely Recent Aerosol Trend, Science, 315, 1543–1543, https://doi.org/10.1126/science.1136709, 2007.

O'Reilly, J. E. and Werdell, P. J.: Chlorophyll algorithms for ocean color sensors - OC4, OC5 & OC6, Remote Sens. Environ., 229, 32–47, https://doi.org/10.1016/j.rse.2019.04.021, 2019.

Pan, X., Ichoku, C., Chin, M., Bian, H., Darmenov, A., Colarco, P., Ellison, L., Kucsera, T., da Silva, A., Wang, J., Oda, T., and Cui, G.: Six global biomass burning emission datasets: intercomparison and application in one global aerosol model, Atmos. Chem. Phys., 20, 969–994, https://doi.org/10.5194/acp-20-969-2020, 2020.

Popp, T., De Leeuw, G., Bingen, C., Brühl, C., Capelle, V., Chedin, A., Clarisse, L., Dubovik, O., Grainger, R., Griesfeller, J., Heckel, A., Kinne, S., Klüser, L., Kosmale, M., Kolmonen, P., Lelli, L., Litvinov, P., Mei, L., North, P., Pinnock, S., Povey, A., Robert, C., Schulz, M., Sogacheva, L., Stebel, K., Stein Zweers, D., Thomas, G., Tilstra, L., Vandenbussche, S., Veefkind, P., Vountas, M., and Xue, Y.: Development, Production and Evaluation of Aerosol Climate Data Records from European Satellite Observations (Aerosol_cci), Remote Sensing, 8, 421, https://doi.org/10.3390/rs8050421, 2016.

Qie, L., Li, Z., Zhu, S., Xu, H., Xie, Y., Qiao, R., Hong, J., and Tu, B.: In-flight radiometric and polarimetric calibration of the Directional Polarimetric Camera onboard the GaoFen-5 satellite over the ocean, Appl. Optics, 60, 7186, https://doi.org/10.1364/ao.422980, 2021.

Ramanathan, V., Crutzen, P. J., Kiehl, J. T., and Rosenfeld, D.: Aerosols, Climate, and the Hydrological Cycle, Science, 294, 2119–2124, https://doi.org/10.1126/science.1064034, 2001.

Satheesh, S. K. and Srinivasan, J.: Enhanced aerosol loading over Arabian Sea during the pre-monsoon season: Natural or anthropogenic?, Geophys. Res. Lett., 29, https://doi.org/10.1029/2002gl015687, 2002.

Sayer, A. M., Hsu, N. C., Bettenhausen, C., Lee, J., Redemann, J., Schmid, B., and Shinozuka, Y.: Extending "Deep Blue" aerosol retrieval coverage to cases of absorbing aerosols above clouds: Sensitivity analysis and first case studies, J. Geophys. Res.-Atmos., 121, 4830–4854, https://doi.org/10.1002/2015jd024729, 2016.

Schaaf, C. B., Gao, F., Strahler, A. H., Lucht, W., Li, X., Tsang, T., Strugnell, N. C., Zhang, X., Jin, Y., Muller, J.-P., Lewis, P., Barnsley, M., Hobson, P., Disney, M., Roberts, G., Dunderdale, M., Doll, C., d'Entremont, R. P., Hu, B., Liang, S., Privette, J. L., and Roy, D.: First operational BRDF, albedo nadir reflectance products from MODIS, Remote Sens. Environ., 83, 135–148, https://doi.org/10.1016/s0034-4257(02)00091-3, 2002.

Schutgens, N., Dubovik, O., Hasekamp, O., Torres, O., Jethva, H., Leonard, P. J. T., Litvinov, P., Redemann, J., Shinozuka, Y., de Leeuw, G., Kinne, S., Popp, T., Schulz, M., and Stier, P.: AEROCOM and AEROSAT AAOD and SSA study – Part 1: Evaluation and intercomparison of satellite measurements, Atmos. Chem. Phys., 21, 6895–6917, https://doi.org/10.5194/acp-21-6895-2021, 2021.

Sinyuk, A., Dubovik, O., Holben, B., Eck, T. F., Breon, F.-M., Martonchik, J., Kahn, R., Diner, D. J., Vermote, E. F., Roger, J.-C., Lapyonok, T., and Slutsker, I.: Simultaneous retrieval of aerosol and surface properties from a combination of AERONET and satellite data, Remote Sens. Environ., 107, 90–108, https://doi.org/10.1016/j.rse.2006.07.022, 2007.

Sinyuk, A., Holben, B. N., Eck, T. F., Giles, D. M., Slutsker, I., Korkin, S., Schafer, J. S., Smirnov, A., Sorokin, M., and Lyapustin, A.: The AERONET Version 3 aerosol retrieval algorithm, associated uncertainties and comparisons to Version 2, Atmos. Meas. Tech., 13, 3375–3411, https://doi.org/10.5194/amt-13-3375-2020, 2020.

Spurr, R. J.: VLIDORT: A linearized pseudo-spherical vector discrete ordinate radiative transfer code for forward model and retrieval studies in multilayer multiple scattering media, J. Quant. Spectrosc. Ra., 102, 316–342, https://doi.org/10.1016/j.jqsrt.2006.05.005, 2006.

Su, X., Wang, L., Zhang, M., Qin, W., and Bilal, M.: A High-Precision Aerosol Retrieval Algorithm (HiPARA) for Advanced Himawari Imager (AHI) data: Development and verification, Remote Sens. Environ., 253, 112221, https://doi.org/10.1016/j.rse.2020.112221, 2021.

Torres, O., Tanskanen, A., Veihelmann, B., Ahn, C., Braak, R., Bhartia, P. K., Veefkind, P., and Levelt, P.: Aerosols and surface UV products from Ozone Monitoring Instrument observations: An overview, J. Geophys. Res.-Atmos., 112, https://doi.org/10.1029/2007jd008809, 2007.

Wang, X., Cai, D., Chen, S., Lou, J., Liu, F., Jiao, L., Cheng, H., Zhang, C., Hua, T., and Che, H.: Spatio-temporal trends of dust emissions triggered by desertification in China, CATENA, 200, 105160, https://doi.org/10.1016/j.catena.2021.105160, 2021.

Wei, X., Cui, Q., Ma, L., Zhang, F., Li, W., and Liu, P.: Global aerosol-type classification using a new hybrid algorithm and Aerosol Robotic Network data, Atmos. Chem. Phys., 24, 5025–5045, https://doi.org/10.5194/acp-24-5025-2024, 2024.

Yang, B., Zhao, H., and Chen, W.: Semi-empirical models for polarized reflectance of land surfaces: Intercomparison using spaceborne POLDER measurements, J. Quant. Spectrosc. Ra., 202, 13–20, https://doi.org/10.1016/j.jqsrt.2017.07.014, 2017.

Yang, X., Zhao, C., Yang, Y., and Fan, H.: Long-term multi-source data analysis about the characteristics of aerosol optical properties and types over Australia, Atmos. Chem. Phys., 21, 3803–3825, https://doi.org/10.5194/acp-21-3803-2021, 2021.

Zhang, L., Li, J., Jiang, Z., Dong, Y., Ying, T., and Zhang, Z.: Clear-Sky Direct Aerosol Radiative Forcing Uncertainty Associated with Aerosol Optical Properties Based on CMIP6 models, J. Climate, 35, 3007–3019, https://doi.org/10.1175/jcli-d-21-0479.1, 2022.

Zhang, Z.: DPC/GaoFen-5 Global Aerosol and Surface Properties Dataset, V1, Peking University Open Research Data Platform [data set], https://doi.org/10.18170/DVN/YMRDFC, 2026.

Zhang, Z., Li, J., Dong, Y., Zhang, C., Ying, T., and Li, Q.: Long-Term Trends in Aerosol Single Scattering Albedo Cause Bias in MODIS Aerosol Optical Depth Trends, IEEE T. Geosci. Remote, 62, 1–9, https://doi.org/10.1109/tgrs.2024.3424981, 2024.

Zhang, Z., Li, J., Che, H., Dong, Y., Dubovik, O., Eck, T., Gupta, P., Holben, B., Kim, J., Lind, E., Saud, T., Tripathi, S. N., and Ying, T.: Long-term trends in aerosol properties derived from AERONET measurements, Atmos. Chem. Phys., 25, 4617–4637, https://doi.org/10.5194/acp-25-4617-2025, 2025a.

Zhang, Z., Li, Z., Fu, G., Hasekamp, O., Fan, C., Qie, L., Xie, Y., Li, L., Ji, Z., and Liu, Q.: Global Aerosol Retrieval Over Land Using the Chinese Satellite Polarimeter DPC-2/GF-5(02), IEEE T. Geosci. Remote, 63, 1–14, https://doi.org/10.1109/tgrs.2025.3633391, 2025b.

Zheng, F., Hou, W., and Li, Z.: Optimal estimation retrieval for directional polarimetric camera onboard Chinese Gaofen-5 satellite: an analysis on multi-angle dependence and a posteriori error, Acta Phys. Sin., 68, 040701, https://doi.org/10.7498/aps.68.20181682, 2019.

Zhu, S., Li, Z., Qie, L., Xu, H., Ge, B., Xie, Y., Qiao, R., Xie, Y., Hong, J., Meng, B., Tu, B., and Chen, F.: In-Flight Relative Radiometric Calibration of a Wide Field of View Directional Polarimetric Camera Based on the Rayleigh Scattering over Ocean, Remote Sensing, 14, 1211, https://doi.org/10.3390/rs14051211, 2022.